# Optimal design of vascular stents using a network of 1D slender curved rods

Sunčica Čanić; Luka Grubišić; Domagoj Lacmanović; Matko Ljulj§and Josip Tambača¶

March 5, 2022

#### Abstract

In this manuscript we present a mathematical theory and a computational algorithm to study optimal design of mesh-like structures such as metallic stents by changing the stent strut thickness and width to optimize the overall stent compliance. The mathematical constrained optimization problem is to minimize the "compliance functional" over a closed and bounded set of constraints. The compliance functional is the stent's overall elastic energy. The constraints are the minimal and maximal strut thickness, and a given fixed volume of the stent material. We prove the existence of a minimizer, thereby proving that the constrained optimization problem has a solution. A numerical scheme based on an iteration procedure is introduced, and implemented within a Finite Element Method framework. Optimal design of three different stent prototypes is considered: (1) a single zig-zag ring, which can be found in many complex stent designs on the US market as a basic cell in the modular stent design, (2) a Palmaz-Schatz type stent consisting of 6 zig-zag rings, and (3) a Cypher(TM) type stent consisting of zig-zag rings with sinusoidal connectors. Several interesting optimization solutions are found, some of which have already been implemented in the design of the currently available stents on the US market. The resulting computational algorithm is compared to a Genetic Algorithm, and it is shown that our computational approach outperforms the Genetic Algorithm in the following three key aspects: (1) computation time, (2) accuracy, and (3) maintaining the symmetry of the solution.

# 1 Introduction

A stent is a metallic mesh tube that acts like a scaffold to help keep arteries open. See Fig. 1. Stents have first been introduced in the late 1980's with the goal to help reduce the resteno-



Figure 1: Photographs of Palmaz stent (left) and Cypher stent (right).

sis rates (re-narrowing of coronary arteries) associated with the angioplasty procedure in the treatment of coronary artery disease. First-generation stents were bare metal stents (BMS) made of 316L stainless steel. BMS are still in use, although with various improved features,

<sup>\*</sup>Department of Mathematics, University of California, Berkeley, canics@berkeley.edu

<sup>&</sup>lt;sup>†</sup>Department of Mathematics, University of Zagreb, luka@math.hr

<sup>&</sup>lt;sup>‡</sup>Department of Mathematics, University of Zagreb, dlacman@math.hr

<sup>§</sup>Department of Mathematics, University of Zagreb, mljulj@math.hr

<sup>¶</sup>Department of Mathematics, University of Zagreb, tambaca@math.hr

including the introduction of materials such as, e.g., cobalt-chromium. BMS reduce the restenosis rates when compared to coronary angioplasty alone, but have been known to cause severe intravascular injuries, often times leading to complications such as in-stent restenosis. In-stent restenosis is associated with damaged and dysfunctional endothelium (the inner-most layer of vascular walls) [42, 10], with vascular inflammation, and with the stretch of the medial layer causing vascular smooth muscle cell injury [23]. The damaged endothelium becomes deficient of antithrombic and antiatherogenic properties, and becomes unable to suppress vascular smooth muscle cell proliferation. Smooth muscle cells start growing inward the blood vessel, causing in-stent restenosis and loss of vessel patency. To further improve the restenosis rates, next generation stents were born with the introduction of drug-eluting stents (DES). DES are stents coated with a polymer which incorporates anti-proliferative drugs (e.g, sirolimus, paclitaxel). The drugs are released slowly over a few weeks after stent deployment. Research has shown that improved geometric and mechanical characteristics of stents can further reduce the restenosis rates [28, 34, 30] both in BMS and in DES, and this remains to be an active area of research [41, 43, 24, 13, 32, 5, 14, 3, 38, 44, 35].

Stents are comprised of struts, distributed on the surface of a cylinder of a certain radius. Balloon expandable stents, which populate the market, are cut out of a slotted tube using a high precision laser. The thickness of the tube and the width of the stent struts affect deliverability, ability to scaffold, radial strength, and disruption of normal flow in the treated coronary artery [37]. In this manuscript we present a mathematical theory and a computational algorithm to study optimal design of mesh-like structures such as metallic stents by changing the stent strut thickness and width to optimize a certain cost function. The goal of the optimization algorithm presented in this manuscript is to find a stent with overall minimal compliance. Different cost functions can be accommodated by this algorithm, such as, e.g., maximal or minimal radial strength, maximal or minimal longitudinal strength, minimal deviation in the  $L^2$ -norm from a given expanded stent shape, etc.

Despite the widespread use of vascular stents, optimal design of their geometric and mechanical properties using a well-defined, rigorous mathematical approach is lacking. The main reason for this is the fact that stents are three-dimensional solids which have been computationally modeled using 3D approaches, see [6, 17, 18, 31, 33, 30, 7, 27, 35] and the references therein. Designing an optimization algorithm based on 3D stent simulations is exceedingly complicated, and often times leads to an algorithm that is computationally very expensive and requires a large memory. Of particular importance in optimal 3D stent design is a very recent work by Russ et al. [35] in which a surrogate-based multi-objective optimization procedure was introduced to study optimal design of a stent that would help anchor a pediatric balloon-expandable heart valve. The approach in [35] relies on 3D simulations of each stent configuration, which is used to generate a surrogate model. While the algorithm is extremely useful, it is also computationally rather expensive (see Section 8 for more information). This is one of the reasons why in [39] the authors of this work introduced a reduced, one-dimensional model to study mesh-like structures such as stents. This model has been rigorously mathematically justified to approximate well the 3D curved rods that comprise a 3D stent, see [39, 20, 12]. The 1D model provides a 3D description of displacements of stent struts using simplified, reduced 1D equations. The reduced model is based on the assumption that stent struts have a small aspect ratio (the ratio of thickness vs. length is small), and can therefore be modeled by the Antman-Cosserat type curved rod model, see [25, 26] for the formal derivation. The curved rods are connected at stent's joints (nodes or vertices) via coupling conditions, such as the continuity of displacement and infinitesimal rotation, and balance of forces and moments, see [40, 20] for the formal derivation. The resulting model is a one-dimensional stent net problem, described in Sec. 2 below. This one-dimensional stent net model is a backbone of the optimization algorithm presented in this manuscript.

The ultimate goal of our research is to design a hybrid algorithm that would identify the

extrema of the cost function using the efficient 1D-based model presented in this manuscript, and then use 3D approaches, such as those presented in Russ et al. [35], to explore a neighborhood around the minumum in order to capture the full 3D information of the optimizer that may not be available from the 1D reduced model approach.

The mathematical constrained optimization problem presented in this manuscript addresses minimization of the "compliance functional" over a closed and bounded set containing the constraints such as the minimal and maximal strut thickness and the total volume of the stent material. Overall, "global" stent compliance is measured by the stent's overall elastic energy. This is presented in Sec. 3. In Sec. 3 we also prove the existence of a minimizer for this problem, thereby proving that the constrained optimization problem has a solution.

To find solutions to the constrained optimization problem we introduce an iteration procedure, described in Sec. 3.1.2 and apply it to different scenarios in terms of optimization parameters, and types of stents. We consider three stent prototypes:

- 1. The Zig-Zag stent, shown in Fig. 2 left, which consists of a single zig-zag ring, which can be found in many complex stent designs as a basic cell in the modular stent design;
- 2. Palmaz-Schatz type stent shown in Fig. 2 middle, which we call Palmaz6 stent due to the six zig-zag rings that comprize the stent;
- 3. Cypher type stent, also known as Bx Velocity(TM), shown in Fig. 2 right, which consists of a sequence of zig-zag rings connected by sinusoidal struts.

The optimization problems for these three stents are solved numerically using a Finite Element Method (FEM) based algorithm, which utilizes a numerical method developed in [21] to study a single one-dimensional stent net problem, formulated in mixed formulation. This algorithm is adapted to the iterative optimization method introduced in this manuscript. It was proved in [22] that the algorithm introduced in [21] converges to the solution of the stent net problem. Details about the numerical method introduced in this manuscript are presented in Sec. 4.

In Sec. 5 we present our numerical results in nine different examples. The results show a number of useful information regarding optimal stent design. In particular, we provide optimal designs with respect to radial stiffness of the three stents considered in this study, which are shown in Fig. 2.

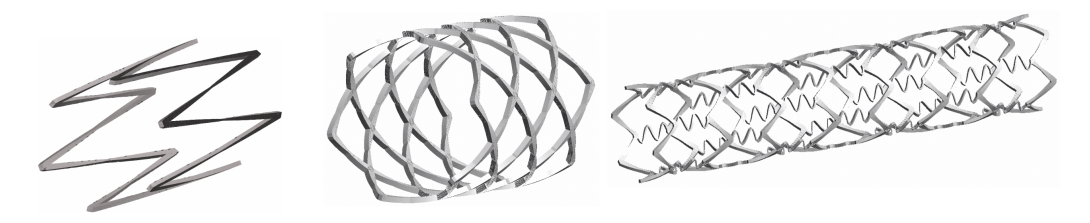


Figure 2: Our numerical results: The three stents considered in this study, optimized with respect to the slotted tube thickness h and struts' thickness w to achieve maximal radial strength. From left to right: the Zig-Zag stent, the Palmaz6 stent, and a Cypher type stent. See Sec. 5 for details.

In Section 6 we compare our algorithm to a genetic algorithm, implemented in Matlab2010a, and show that the algorithm proposed in this manuscript outperforms the genetic algorithm in three key aspects: (1) computational time, (2) accuracy, and (3) maintaining the symmetry of the solution.

To gain an insight into the strain distribution in the non-optimized and optimized stent configurations, in Sec. 7 we present the strain results for the three stents shown above. We show that the maximum strain for the optimized Palmaz6 and Cypher stents is significantly lower than that of the non-optimized configuration, while the maximal strain does not change in a significant way for the optimized single zig-zag ring.

We conclude this manuscript with a summary of the results and a few remarks comparing the method discussed in this manuscript with the 3D surrogate-based modeling, presented in the work by Russ et al. in [35].

# 2 The stent model

#### 2.1 Differential formulation

A stent is a three-dimensional elastic body defined to be a union of three-dimensional struts. To formulate an algorithm for optimal stent design, we adopt the approach proposed in [39] where stents are modeled as one-dimensional nets/networks. The slender stent struts are modeled as one-dimensional curved rods, satisfying certain contact conditions at the locations where the stent struts meet. Details of the one-dimensional stent net model are presented next.

# 2.1.1 The geometry

The reduced, one-dimensional stent net model is defined on a graph domain, where the edges of the graph correspond to the middle lines of the curved rods (stent struts), and the vertices of the graph correspond to the points where the curved rods (stent struts) meet. The following notation will be used in the definition of the one-dimensional, reduced stent model:

- $\mathcal{V}$  denotes the set of  $n_{\mathcal{V}}$  vertices in a stent (points where stent struts' middle lines meet);
- $\mathcal{E}$  denotes the set of  $n_{\mathcal{E}}$  edges (pairing of vertices) corresponding to the middle lines;
- $\Phi^i: [0, \ell_i] \to \mathbb{R}^3$  denotes the natural parametrization of the middle line of the *i*th strut, i.e., edge  $e_i \in \mathcal{E}, i = 1, \dots, n_{\mathcal{E}}$ ;
- $n^i, b^i$  denotes the orthonormal basis in the normal plane of  $\Phi^i$ , see Fig. 3; together with the tangential vector  $t^i = (\Phi^i)'$  they form the Frenet basis of the *i*th strut;
- $\mu_i, \lambda_i, E_i = \mu^i (3\lambda^i + 2\mu^i)/(\lambda^i + \mu^i)$  are the material parameters (Lamé constants, and Young's modulus, respectively) associated with the *i*th strut,  $i = 1, \ldots, n_{\mathcal{E}}$ ;
- $I_{\alpha,\beta}^i$  (where  $\alpha,\beta=1,2$ ) and  $K^i$  are moments of inertia and torsional rigidity, respectively, of cross-sections of the *i*th strut,  $i=1,\ldots,n_{\mathcal{E}}$ .

The ordered pair  $\mathcal{N} = (\mathcal{V}, \mathcal{E})$  defines a stent graph and sets the topology of the stent. The stent geometry is made precise by the parameterizations  $\Phi^i$  for each  $i = 1, \dots, n_{\mathcal{E}}$ , which introduce orientation on the graph. Since the mechanical behavior of stents is *independent* of orientation, it is reasonable to expect that the resulting problem will be independent of graph's orientation. Indeed, we will see below that this is the case. Since this is different from classical network problems in which orientation is important (e.g., channel flow), the stent problem is called the stent *net* problem [39, 11].

# 2.1.2 The elasticity equations

The one-dimensional stent net model describing the mechanical behavior of a given three-dimensional stent is defined by a family of 1D curved rod equations given in terms of the parameterization parameter  $s \in [0, l_i]$  for each edge  $e_i$ , supplemented by a set of coupling conditions holding at each stent vertex where the edges meet. The 1D curved rod equations for the curved rod (edge)  $e_i$  are given in terms of the following unknown functions:

- $u^i: [0, \ell^i] \to \mathbb{R}^3$ , the displacement of the middle curve of the rod  $e_i$ ;
- $\omega^i:[0,\ell^i]\to\mathbb{R}^3$ , infinitesimal rotation of the cross-section of the rod  $e_i$ ;
- $q^i:[0,\ell^i]\to\mathbb{R}^3$ , contact moment associated with  $e_i$ ;
- $p^i:[0,\ell^i]\to\mathbb{R}^3$ , contact force associated with  $e_i$ .

For a given stent loading, given by the line force density  $f^i$ , the equations read [39]:

$$0 = \partial_s \boldsymbol{p}^i + \boldsymbol{f}^i, \tag{2.1}$$

$$0 = \partial_s \mathbf{q}^i + \mathbf{t}^i \times \mathbf{p}^i, \tag{2.2}$$

$$0 = \partial_s \boldsymbol{\omega}^i - \mathbf{Q}^i (\mathbf{H}^i)^{-1} (\mathbf{Q}^i)^T \boldsymbol{q}^i, \tag{2.3}$$

$$0 = \partial_s \boldsymbol{u}^i + \boldsymbol{t}^i \times \boldsymbol{\omega}^i, \tag{2.4}$$

for each  $e_i \in \mathcal{E}$ ,  $i = 1, ..., n_{\mathcal{E}}$ . Here,  $\mathbf{H}^i$  and  $\mathbf{Q}^i$  are matrices given by

$$\mathbf{H}^{i} = \begin{bmatrix} \mu^{i} K^{i} & 0 & 0 \\ 0 & E^{i} I_{33}^{i} & E^{i} I_{23}^{i} \\ 0 & E^{i} I_{23}^{i} & E^{i} I_{22}^{i} \end{bmatrix}, \qquad \mathbf{Q}^{i} = \begin{bmatrix} \mathbf{t}^{i} & \mathbf{n}^{i} & \mathbf{b}^{i} \end{bmatrix},$$
(2.5)

see e.g. [9]. For a given cross-section S,  $I_{\alpha\alpha}$  are moments of inertia,  $I_{23}$  is the product of inertia, and K is torsional rigidity of the cross-section S, i.e.,

$$I_{\alpha\beta} = (-1)^{\alpha\beta} \int_{S} z_{\alpha} z_{\beta} dz_{2} dz_{3}, \quad \alpha, \beta \in \{2, 3\}, \qquad K = \int_{S} (\partial_{2} w - z_{3})^{2} + (\partial_{3} w + z_{2})^{2} dz_{2} dz_{3}. \quad (2.6)$$

Here, we denoted by  $z_2$  and  $z_3$  the local normal and bi-normal variables, see Fig. 3, and w is called the warping function, which is defined as the unique solution of the Neumann problem: find  $w \in H^1(S)$  such that

$$\int_{S} (\partial_2 w - z_3) \partial_2 r + (\partial_3 w + z_2) \partial_3 r = 0, \quad r \in H^1(S), \qquad \int_{S} w = 0.$$

Matrix  $\mathbf{H}^i$  describes the elastic properties of the *i*-th rod and the geometry of its cross-section, and matrix  $\mathbf{Q}^i$  describes the local geometry of the *i*-th rod parametried by  $\mathbf{\Phi}^i$ , up to translations;  $\mathbf{t}^i = (\mathbf{\Phi}^i)'$  is the unit tangent vector to the curve parametrized by  $\mathbf{\Phi}^i$ , while  $\mathbf{n}^i$  and  $\mathbf{b}^i$  constitute one orthonormal basis in the normal plane to the middle curve of the *i*th rod. See Fig. 3.

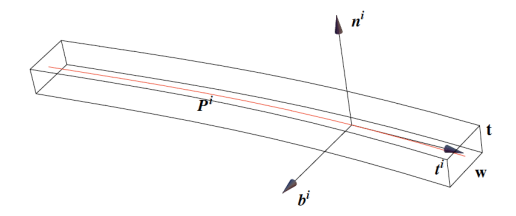


Figure 3: One stent strut with the tangential, normal and binormal vectors to the middle line.

### 2.1.3 The coupling conditions

To complete the problem, we need to prescribe the physics of the coupling between the stent struts at the points where they meet, namely, the coupling conditions corresponding to (2.1)-(2.4) at each vertex of the stent net. Two sets of coupling conditions, known as the kinematic

and dynamic coupling conditions, give rise to a well-defined problem. They are defined in terms of the set  $J_j^-$  of all the outgoing edges for the vertex j where the local variable s is equal to 0, and the set  $J_j^+$  of all the incoming edges where the local variable s is equal to  $\ell$ . The conditions read:

(KC) The kinematic conditions which state that  $(u, \omega)$  are continuous at each vertex:

$$\boldsymbol{\omega}^{i}(0) = \boldsymbol{\omega}^{k}(\ell_{k}), \qquad i \in J_{j}^{-}, k \in J_{j}^{+}, \qquad j = 1, \dots, n_{\mathcal{V}},$$
  
$$\boldsymbol{u}^{i}(0) = \boldsymbol{u}^{k}(\ell_{k}), \qquad i \in J_{j}^{-}, k \in J_{j}^{+}, \qquad j = 1, \dots, n_{\mathcal{V}}.$$

$$(2.7)$$

(DC) The dynamic conditions which require balance of contact forces p and contact moments q at each vertex:

$$\sum_{i \in J_j^+} \mathbf{p}^i(\ell_i) - \sum_{i \in J_j^-} \mathbf{p}^i(0) = 0, \qquad j = 1, \dots, n_{\mathcal{V}},$$

$$\sum_{i \in J_j^+} \mathbf{q}^i(\ell_i) - \sum_{i \in J_j^-} \mathbf{q}^i(0) = 0, \qquad j = 1, \dots, n_{\mathcal{V}}.$$
(2.8)

Since the problem is a pure traction problem, solutions are unique up to a translation and rotation. To fix the unique solution, zero total translation and zero total rotation are prescribed:

$$\sum_{i=1}^{n_{\mathcal{E}}} \int_0^{\ell_i} \mathbf{u}^i ds = \sum_{i=1}^{n_{\mathcal{E}}} \int_0^{\ell_i} \boldsymbol{\omega}^i ds = 0.$$
 (2.9)

# 2.2 Weak formulation: the classical and mixed forms

We start by introducing a mixed weak formulation, which will be used in the numerical simulations. The mixed formulation is necessary to account for the conditions of inextensibility and unshearbility of each rod. For this purpose, we introduce a vector function  $\mathbf{u}_S$ , where the subscript S stands for "stent", to denote the state variables  $(\mathbf{u}^i, \boldsymbol{\omega}^i)$  defined on all the edges  $e^i, i = 1, ..., n_{\mathcal{E}}$  of a given stent, so that

$$m{u}_S = ((m{u}^1, m{\omega}^1), ..., (m{u}^{n_{\mathcal{E}}}, m{\omega}^{n_{\mathcal{E}}})) =: (m{y}^1, ..., m{y}^{n_{\mathcal{E}}}).$$

The kinematic coupling condition requires that the displacements  $u^i$  of the middle lines, and the infinitesimal rotations  $\omega^i$  of the cross-sections, are continuous at every vertex  $V \in \mathcal{V}$ . We include this condition in the solutions space:

$$H^{1}(\mathcal{N}; \mathbb{R}^{6}) = \left\{ \boldsymbol{u}_{S} = (\boldsymbol{y}^{1}, \dots, \boldsymbol{y}^{n_{\mathcal{E}}}) \in \prod_{i=1}^{n_{\mathcal{E}}} H^{1}(0, \ell_{i}; \mathbb{R}^{6}) : \right.$$
$$\boldsymbol{y}^{i}(0) = \boldsymbol{y}^{k}(\ell_{k}), \forall i \in J_{j}^{-}, k \in J_{j}^{+}, j = 1, \dots, n_{\mathcal{V}} \right\}.$$

Thus, the kinematic coupling conditions will be satisfied in the strong sense. In contrast, the dynamic coupling conditions will be imposed weakly, in the weak formulation of the problem, through integration by parts.

To get to the weak formulation of the stent problem, we recall that a stent is a union of stent struts. Thus, the (mixed) weak formulation of the entire stent is obtained by adding up the (mixed) weak formulations of each stent strut. We will do this for the functions  $\mathbf{u}_S \in V_s$  and  $\mathbf{p}_S := (\mathbf{p}^1, \dots, \mathbf{p}^{n\varepsilon}, \boldsymbol{\alpha}, \boldsymbol{\beta}) \in Q_S$ , where

$$V_S = H^1(\mathcal{N}; \mathbb{R}^6), \qquad Q_S = L^2(\mathcal{N}; \mathbb{R}^3) \times \mathbb{R}^3 \times \mathbb{R}^3 = \prod_{i=1}^{n_{\mathcal{E}}} L^2(0, \ell_i; \mathbb{R}^3) \times \mathbb{R}^3 \times \mathbb{R}^3.$$

These functions are defined on the entire stent, and the state variables  $u_S$  are continuous at vertices (globally continuous). The functions  $p_S$  play the role of Lagrange multipliers, enforcing the inextensibility and unshearability condition (2.4), and zero total translation and rotation (see below).

After multiplying the differential equations (2.1)-(2.2) by the components of the test functions  $\tilde{\boldsymbol{u}}_S$ , and integrating them by parts, and after using the dynamic coupling conditions into account at stent's vertices, the resulting mixed weak formulation can be written in terms of the bilinear forms  $k_S: V_S \times V_S \to \mathbb{R}$  and  $b_S: Q_S \times V_S \to \mathbb{R}$ , where:

$$k_{S}(\boldsymbol{u}_{S}, \tilde{\boldsymbol{u}}_{S}) = \sum_{i=1}^{n_{\mathcal{E}}} \int_{0}^{\ell_{i}} \mathbf{Q}^{i} \mathbf{H}^{i}(\mathbf{Q}^{i})^{T} \partial_{s} \boldsymbol{\omega}^{i} \cdot \partial_{s} \tilde{\boldsymbol{\omega}}^{i} ds,$$

$$b_{S}(\boldsymbol{p}_{S}, \tilde{\boldsymbol{u}}_{S}) = \sum_{i=1}^{n_{\mathcal{E}}} \int_{0}^{\ell_{i}} \boldsymbol{p}^{i} \cdot (\partial_{s} \tilde{\boldsymbol{u}}^{i} + \boldsymbol{t}^{i} \times \tilde{\boldsymbol{\omega}}^{i}) ds + \boldsymbol{\alpha} \cdot \sum_{i=1}^{n_{\mathcal{E}}} \int_{0}^{\ell_{i}} \tilde{\boldsymbol{u}}^{i} ds + \boldsymbol{\beta} \cdot \sum_{i=1}^{n_{\mathcal{E}}} \int_{0}^{\ell_{i}} \tilde{\boldsymbol{\omega}}^{i} ds.$$

$$(2.10)$$

To deal with the source term, the following linear functional is introduced:

$$l_S: V_S \to \mathbb{R}, \qquad l_S(\tilde{\boldsymbol{u}}_S) = \sum_{i=1}^{n_{\mathcal{E}}} \int_0^{\ell_i} \boldsymbol{f}^i \cdot \tilde{\boldsymbol{u}}^i ds.$$
 (2.11)

The mixed formulation of our problem is then given by: find  $(u_S, p_S) \in V_S \times Q_S$  such that

$$k_S(\boldsymbol{u}_S, \tilde{\boldsymbol{u}}_S) + b_S(\boldsymbol{p}_S, \tilde{\boldsymbol{u}}_S) = l_S(\tilde{\boldsymbol{u}}_S), \quad \forall \tilde{\boldsymbol{u}}_S \in V_S, b_S(\tilde{\boldsymbol{p}}_S, \boldsymbol{u}_S) = 0, \quad \forall \tilde{\boldsymbol{p}}_S \in Q_S.$$

$$(2.12)$$

The existence of a unique solution to this problem was proved in [21].

To get to the classical weak formulation, we introduce the space:

$$V_S^{\mathrm{Ker}} = \{ \tilde{\boldsymbol{u}}_S \in V_S : b_S(\tilde{\boldsymbol{p}}_S, \tilde{\boldsymbol{u}}_S) = 0, \tilde{\boldsymbol{p}}_S \in Q_S \}.$$

The classical **weak formulation** then reads: find  $oldsymbol{u}_S \in V_S^{\operatorname{Ker}}$  such that

$$k_S(\boldsymbol{u}_S, \tilde{\boldsymbol{u}}_S) = l_S(\tilde{\boldsymbol{u}}_S), \quad \forall \tilde{\boldsymbol{u}}_S \in V_S^{\text{Ker}},$$
 (2.13)

where the left-hand side corresponds to the elastic energy of the stent. It was shown in [21] that the weak formulation and the mixed formulation above are equivalent. This is because the form  $k_S$  is coercive on  $V_S^{\text{Ker}}$ , and b satisfies the inf-sup condition from Brezzi and Fortin [8].

In this work we will consider optimal design of stents with respect to the change in the slotted tube thickness h, and the stent strut's width w, by considering the following scenarios:

- 1. Square cross-sections: We assume that h = w and optimize the overall, global stent stiffness by simultaneously changing h and w so that h = w;
- 2. Rectangular cross-sections: We optimize the overall, global stent stiffness in the following two sub-cases:
  - (A) We keep the thickness h of the slotted tube fixed, and only optimize with respect to the width w of the stent struts;
  - (B) We vary both h and w, but keep the thickness h constant along the entire stent.

For some topology optimization problems of lattice structures, see e.g. [15, 16].

The mathematical constrained optimization problem is presented next.

# 3 The constrained optimization problem

To define a constrained optimization problem in terms of h and w, we need to understand the dependence of the problem on those parameters. We will be working with the mixed formulation given in (2.12), where h and w appear in the matrices  $\mathbf{H}^i$ , defined in (2.5).

To see how the coefficients of  $\mathbf{H}^i$  (the *i*th strut) depend on the parameters h (thickness of the tube) and w (width of stent struts), we recall the definitions (2.6) of the moments of inertia  $I_{\alpha,\beta}$  and of torsional rigidity K. For a **rectangular** cross-section  $S = \left[-\frac{1}{2}h, \frac{1}{2}h\right] \times \left[-\frac{1}{2}w, \frac{1}{2}w\right]$  we get:

$$I_{23} = 0,$$
  $I_{22} = \int_{S} (z_2)^2 dz_2 dz_3 = \frac{1}{12} w h^3,$   $I_{33} = \int_{S} (z_3)^2 dz_2 dz_3 = \frac{1}{12} w^3 h,$ 

and

$$K = \frac{1}{3}hw\left(\frac{h^2}{4} + \frac{w^2}{4}\right) + 32\sum_{k=1}^{\infty} \frac{1}{(2k-1)^5\pi^5} \left((2k-1)\pi hw\left(\frac{h^2}{4} + \frac{w^2}{4}\right) - w^4 \tanh\frac{(2k-1)\pi h}{2w} - h^4 \tanh\frac{(2k-1)\pi w}{2h}\right).$$
(3.1)

In the case of a **square** cross section, w is set equal to h, in which case the cross-section can be scaled by h with respect to its center of mass, i.e.,  $S^{i}(h) = h\tilde{S}^{i}$ , and the matrix  $\mathbf{H}^{i}(h)$  then scales like  $h^{4}$ , i.e.,

$$\mathbf{H}^i(h) = h^4 \tilde{\mathbf{H}}^i,$$

where  $\tilde{\mathbf{H}}^i$  is the matrix defined as in (2.5) and (2.6), but for  $\tilde{S}^i$  instead of  $S^i$ .

In the following three subsections we present the three optimization algorithms, corresponding to the scenarios (1), (2A) and (2B) above.

### 3.1 Square cross-sections: perturbations with respect to the square side h

Here, we assume that the struts' cross-sections are squares with a constant  $h^i$  along the entire i-th strut, for each  $i = 1, \ldots, n_{\mathcal{E}}$ . This implies that

$$\mathbf{H}^i = (h^i)^4 \tilde{\mathbf{H}}^i, \qquad i = 1, \dots, n_{\mathcal{E}},$$

for matrices  $\tilde{\mathbf{H}}^i$  that do not depend on strut thickness.

We will be assuming that the stent loading, given by  $f^i$ ,  $i = 1..., n_{\mathcal{E}}$ , is independent of the stent strut thickness. This is a natural assumption in applications, since the stent loading comes from the forces exerted by the blood vessel walls onto the stent, which is independent of the stent strut thickness.

Therefore for a given thickness function  $\mathbf{h} = (h^1, \dots, h^{n_{\mathcal{E}}})$ , the mixed formulation for the stent model, written explicitly in terms of  $\mathbf{h}$ , is given by: find  $(\mathbf{u}_S(\mathbf{h}), \mathbf{p}_S(\mathbf{h})) \in V_S \times Q_S$ , such that

$$k_S(\boldsymbol{h})(\boldsymbol{u}_S, \tilde{\boldsymbol{u}}_S) + b_S(\boldsymbol{p}_S, \tilde{\boldsymbol{u}}_S) = l_S(\tilde{\boldsymbol{u}}_S), \quad \tilde{\boldsymbol{u}}_S \in V_S, b_S(\tilde{\boldsymbol{p}}_S, \boldsymbol{u}_S) = 0, \quad \tilde{\boldsymbol{p}}_S \in Q_S,$$

$$(3.2)$$

where  $k_S(\mathbf{h})$  is given in (2.10) with  $\mathbf{H}^i$  replaced by  $(h^i)^4 \tilde{\mathbf{H}}^i$ .

We consider an optimization problem in which the **cost function** is the stent's overall **compliance**. Compliance is measured by the stent's overall elastic energy. See (2.13). For example, to find a stent with minimal compliance, we seek to minimize the elastic energy of the stent in such a way that the resulting displacement, for a given outside forcing, satisfies the stent problem (3.2). Since the elastic energy for a given forcing must be equal  $\int_{\mathcal{N}} \mathbf{f} \cdot \mathbf{u}_S ds$ , see (2.13),

we introduce the following **cost function**  $J: V_S \times Q_S \to \mathbb{R}$  for the problem of optimizing the overall stent's compliance:

$$J(\boldsymbol{u}_S, \boldsymbol{p}_S) = \int_{\mathcal{N}} \boldsymbol{f} \cdot \boldsymbol{u}_S ds = \sum_{i=1}^{n_{\mathcal{E}}} \int_0^{\ell^i} \boldsymbol{f}^i \cdot \boldsymbol{u}^i ds, \tag{3.3}$$

where  $(u_S, p_S)$  is the solution of (3.2). For a given value  $h : \mathcal{N} \to \mathbb{R}$ , which is constant for each stent strut, we denote by  $(u_S(h), p_S(h))$  the solution of (3.2). The **optimal stent design problem** now reads as follows:

Find  $\boldsymbol{h}^* \in \mathbb{R}^{n_{\mathcal{E}}}$  such that

$$\begin{cases}
J(\boldsymbol{u}_{S}(\boldsymbol{h}^{*}), \boldsymbol{p}_{S}(\boldsymbol{h}^{*})) = \min_{\boldsymbol{h} \in W} J(\boldsymbol{u}_{S}(\boldsymbol{h}), \boldsymbol{p}_{S}(\boldsymbol{h})), \\
\text{where } (\boldsymbol{u}_{S}(\boldsymbol{h}), \boldsymbol{p}_{S}(\boldsymbol{h})) \text{ is the unique solution of } (3.2),
\end{cases}$$
(3.4)

where  $J(\boldsymbol{u}_S(\boldsymbol{h}), \boldsymbol{p}_S(\boldsymbol{h}))$  is given by (3.3).

The set  $W \subset \mathbb{R}^{n_{\mathcal{E}}}$  contains **constraints**, such as, e.g., the minimal and maximal stent strut thickness,  $0 < h_{\min} \le h^i \le h_{\max}$ , and a constraint on the total volume  $V_0$  of the material the stent is made of. Indeed, we take the set of constraints W to be:

$$W = \{ \boldsymbol{h} \in \mathbb{R}^{n_{\mathcal{E}}} : h_{\min} \le h^i \le h_{\max}, i = 1, \dots, n_{\mathcal{E}}, \sum_{i=1}^{n_{\mathcal{E}}} (h^i)^2 \ell^i = V_0 \}.$$
 (3.5)

Since the set  $W \subset \mathbb{R}^{n_{\mathcal{E}}}$  is bounded and closed we will be able to prove the existence of a solution to (3.4).

### **3.1.1** Existence of a minimizer defined by (3.4)

The existence of a minimizer is based on the properties of the set W, and on the continuity properties of the function J as a function of h. To analyze the properties of J in terms of h, we introduce the following notation denoting explicit dependence of J on h:

$$\tilde{J}(\boldsymbol{h}) := J(\boldsymbol{u}_S(\boldsymbol{h}), \boldsymbol{p}_S(\boldsymbol{h})) = \sum_{i=1}^{n_{\mathcal{E}}} \int_0^{\ell^i} \boldsymbol{f}^i \cdot \boldsymbol{u}^i(\boldsymbol{h}) ds, \tag{3.6}$$

where  $(\boldsymbol{u}_S(\boldsymbol{h}), \boldsymbol{p}_S(\boldsymbol{h}))$  is the solution of (3.2). Thus, to show continuity of  $\boldsymbol{h} \mapsto \tilde{J}(\boldsymbol{h})$ , it is enough to prove that  $\boldsymbol{h} \mapsto \boldsymbol{u}(\boldsymbol{h})$  is continuous. To show that  $\boldsymbol{u}$  depends continuously on  $\boldsymbol{h}$ , we consider the family  $(\boldsymbol{h}_{\lambda})_{\lambda}$  and functions  $(\boldsymbol{u}_S(\boldsymbol{h}_{\lambda}), \boldsymbol{p}_S(\boldsymbol{h}_{\lambda}))_{\lambda}$ , where  $(\boldsymbol{u}_S(\boldsymbol{h}_{\lambda}), \boldsymbol{p}_S(\boldsymbol{h}_{\lambda}))$  is a unique solution of (3.2), and we show that when  $\boldsymbol{h}_{\lambda} \to \boldsymbol{h}$ , the family  $(\boldsymbol{u}_S(\boldsymbol{h}_{\lambda}), \boldsymbol{p}_S(\boldsymbol{h}_{\lambda}))_{\lambda}$  converges to the solution  $(\boldsymbol{u}_S(\boldsymbol{h}), \boldsymbol{p}_S(\boldsymbol{h}))$ . More precisely, we have the following theorem.

**Theorem 3.1** (Continuity). Let  $(\mathbf{u}_S(\mathbf{h}), \mathbf{p}_S(\mathbf{h}))$  be a family (parameterized by  $\mathbf{h}$ ) of unique solutions of (3.2). Then, for each fixed  $\mathbf{h}$ , the family of solutions  $(\mathbf{u}_S(\mathbf{h}_{\lambda}), \mathbf{p}_S(\mathbf{h}_{\lambda}))_{\lambda}$  converges strongly in  $H^1(\mathcal{N}; \mathbb{R}^6) \times L^2(\mathcal{N}; \mathbb{R}^3)$  to the solution  $(\mathbf{u}_S(\mathbf{h}), \mathbf{p}_S(\mathbf{h}))$  as  $\mathbf{h}_{\lambda} \to \mathbf{h}$ .

*Proof.* To prove this theorem we first recall that  $(\boldsymbol{u}_S(\boldsymbol{h}_{\lambda}), \boldsymbol{p}_S(\boldsymbol{h}_{\lambda}))_{\lambda}$  satisfy the mixed formulation (3.2). To emphasize the dependence on  $\lambda$ , we introduce the notation  $\langle \boldsymbol{F}_{\lambda}, \tilde{\boldsymbol{u}}_S \rangle$  instead of  $l_S(\tilde{\boldsymbol{u}}_S)$ , and write (3.2) in terms of this new notation as

$$k_{S}(\boldsymbol{h}_{\lambda})(\boldsymbol{u}_{S}(\boldsymbol{h}_{\lambda}), \tilde{\boldsymbol{u}}_{S}) + b_{S}(\boldsymbol{p}_{S}(\boldsymbol{h}_{\lambda}), \tilde{\boldsymbol{u}}_{S}) = \langle \boldsymbol{F}_{\lambda}, \tilde{\boldsymbol{u}}_{S} \rangle, \quad \tilde{\boldsymbol{u}}_{S} \in V_{S},$$

$$b_{S}(\tilde{\boldsymbol{p}}_{S}, \boldsymbol{u}_{S}(\boldsymbol{h}_{\lambda})) = 0, \quad \tilde{\boldsymbol{p}}_{S} \in Q_{S}.$$

$$(3.7)$$

We now show that solutions  $(\boldsymbol{u}_S(\boldsymbol{h}_{\lambda}), \boldsymbol{p}_S(\boldsymbol{h}_{\lambda}))_{\lambda}$  of this mixed formulation, are uniformly bounded (uniformly in  $\lambda$ ), which will be used to prove  $(\boldsymbol{u}_S(\boldsymbol{h}_{\lambda}) - \boldsymbol{u}(\boldsymbol{h}), \boldsymbol{p}_S(\boldsymbol{h}_{\lambda}) - \boldsymbol{p}(\boldsymbol{h})) \to 0$  in  $H^1(\mathcal{N}; \mathbb{R}^6) \times L^2(\mathcal{N}; \mathbb{R}^3)$ , as  $\boldsymbol{h}_{\lambda} \to \boldsymbol{h}$ . In fact, we prove the following more general result.

**Lemma 3.2.** Let  $(f_{(1,\lambda)}, f_{(2,\lambda)}, f_{(3,\lambda)}, f_{(4,\lambda)})_{\lambda}$  be a family of source terms in  $L^2(\mathcal{N}; \mathbb{R}^3)^4$  and  $(h_{\lambda})_{\lambda} \subset W$ . For each  $\tilde{\boldsymbol{u}}_S \in V_S$  denote

$$\langle m{F}_{\lambda}, m{ ilde{u}}_{S} 
angle = \sum_{i=1}^{n_{\mathcal{E}}} \int_{0}^{\ell^{i}} \left( m{f}_{(1,\lambda)}^{i} \cdot m{ ilde{u}}^{i} + m{f}_{(2,\lambda)}^{i} \cdot \partial_{s} m{ ilde{u}}^{i} + m{f}_{(3,\lambda)}^{i} \cdot m{ ilde{\omega}}^{i} + m{f}_{(4,\lambda)}^{i} \cdot \partial_{s} m{ ilde{\omega}}^{i} 
ight) ds.$$

Let  $(\boldsymbol{u}_S^{\boldsymbol{h}_{\lambda}}, \boldsymbol{p}_S^{\boldsymbol{h}_{\lambda}})_{\lambda} \subset V_S \times Q_S$  be the solutions of problems

$$k_{S}(\boldsymbol{h}_{\lambda})(\boldsymbol{u}_{S}^{\boldsymbol{h}_{\lambda}}, \tilde{\boldsymbol{u}}_{S}) + b_{S}(\boldsymbol{p}_{S}^{\boldsymbol{h}_{\lambda}}, \tilde{\boldsymbol{u}}_{S}) = \langle \boldsymbol{F}_{\lambda}, \tilde{\boldsymbol{u}}_{S} \rangle, \quad \tilde{\boldsymbol{u}}_{S} \in V_{S},$$

$$b_{S}(\tilde{\boldsymbol{p}}_{S}, \boldsymbol{u}_{S}^{\boldsymbol{h}_{\lambda}}) = 0, \quad \tilde{\boldsymbol{p}}_{S} \in Q_{S}.$$

$$(3.8)$$

1. If there exists C > 0 such that  $||f_{(i,\lambda)}||_{L^2(\mathcal{N};\mathbb{R}^3)} \leq C$  (independent of  $\lambda$ ), for i = 1, 2, 3, 4, then there exists C' > 0 such that

$$\|m{u}_S^{m{h}_{\lambda}}\|_{H^1(\mathcal{N};\mathbb{R}^6)}, \ \|m{p}_S^{m{h}_{\lambda}}\|_{L^2(\mathcal{N};\mathbb{R}^3)} \leq C'.$$

2. If  $\mathbf{f}_{(i,\lambda)} \to 0$  in  $L^2(\mathcal{N}; \mathbb{R}^3)$  as  $\mathbf{h}_{\lambda} \to \mathbf{h}$ , for i = 1, 2, 3, 4, then

$$oldsymbol{u}_S^{oldsymbol{h}_\lambda} o 0 \ in \ H^1(\mathcal{N};\mathbb{R}^6), \quad oldsymbol{p}_S^{oldsymbol{h}_\lambda} o 0 \ in \ L^2(\mathcal{N};\mathbb{R}^3).$$

We will prove this lemma after we finish the proof of Theorem 3.1.

From the first part of this lemma, applied to the case  $f_{(2,\lambda)} = f_{(3,\lambda)} = f_{(4,\lambda)} = 0$  and for  $f_{(1,\lambda)}$  independent of  $\lambda$ , we obtain that the family  $(\boldsymbol{u}_S(\boldsymbol{h}_{\lambda}), \boldsymbol{p}_S(\boldsymbol{h}_{\lambda})_{\lambda})$  is uniformly bounded in  $H^1(\mathcal{N}; \mathbb{R}^6) \times L^2(\mathcal{N}; \mathbb{R}^3)$  by a constant M > 0.

We now use this to show that  $(\mathbf{u}_S(\mathbf{h}_{\lambda}) - \mathbf{u}(\mathbf{h}), \mathbf{p}_S(\mathbf{h}_{\lambda}) - \mathbf{p}(\mathbf{h})) \to 0$ . For this purpose, we derive a system of equations that is satisfied by the difference  $(\mathbf{u}_S(\mathbf{h}_{\lambda}) - \mathbf{u}(\mathbf{h}), \mathbf{p}_S(\mathbf{h}_{\lambda}) - \mathbf{p}(\mathbf{h}))$ , and show that the system is of the form (3.8). Indeed, by recalling the left hand-side of (3.2), we obtain:

$$k_S(\boldsymbol{h})(\boldsymbol{u}_S(\boldsymbol{h}_{\lambda}) - \boldsymbol{u}_S(\boldsymbol{h}), \tilde{\boldsymbol{u}}_S) + b_S(\boldsymbol{p}_S(\boldsymbol{h}_{\lambda}) - \boldsymbol{p}_S(\boldsymbol{h}), \tilde{\boldsymbol{u}}_S)$$
  
=  $k_S(\boldsymbol{h})(\boldsymbol{u}_S(\boldsymbol{h}_{\lambda}), \tilde{\boldsymbol{u}}_S) + b_S(\boldsymbol{p}_S(\boldsymbol{h}_{\lambda}), \tilde{\boldsymbol{u}}_S) - l_S(\tilde{\boldsymbol{u}}_S),$ 

where we have used the fact that  $\mathbf{u}_S(\mathbf{h})$  is a solution to (3.2). The last two terms on the right hand-side can be further rewritten as  $-k_S(\mathbf{h}_{\lambda})(\mathbf{u}_S(\mathbf{h}_{\lambda}), \tilde{\mathbf{u}}_S)$  by recalling that  $\mathbf{u}_S(\mathbf{h}_{\lambda})$  is also a solution to (3.2). Thus, we obtain:

$$k_{S}(\boldsymbol{h})(\boldsymbol{u}_{S}(\boldsymbol{h}_{\lambda}) - \boldsymbol{u}_{S}(\boldsymbol{h}), \tilde{\boldsymbol{u}}_{S}) + b_{S}(\boldsymbol{p}_{S}(\boldsymbol{h}_{\lambda}) - \boldsymbol{p}_{S}(\boldsymbol{h}), \tilde{\boldsymbol{u}}_{S})$$

$$= k_{S}(\boldsymbol{h})(\boldsymbol{u}_{S}(\boldsymbol{h}_{\lambda}), \tilde{\boldsymbol{u}}_{S}) - k_{S}(\boldsymbol{h}_{\lambda})(\boldsymbol{u}_{S}(\boldsymbol{h}_{\lambda}), \tilde{\boldsymbol{u}}_{S})$$

$$= \sum_{i=1}^{n_{\mathcal{E}}} ((h^{i})^{4} - (h^{i}_{\lambda})^{4}) \int_{0}^{\ell^{i}} \mathbf{Q}^{i} \tilde{\mathbf{H}}^{i}(\mathbf{Q}^{i})^{T} \partial_{s} \boldsymbol{\omega}^{i}(\boldsymbol{h}_{\lambda}) \cdot \partial_{s} \tilde{\boldsymbol{\omega}}^{i} ds.$$

Therefore,  $(u_S(h_\lambda) - u(h), p_S(h_\lambda) - p(h))$  satisfies the following system of two equations:

$$k_{S}(\boldsymbol{h})(\boldsymbol{u}_{S}(\boldsymbol{h}_{\lambda}) - \boldsymbol{u}_{S}(\boldsymbol{h}), \tilde{\boldsymbol{u}}_{S}) + b_{S}(\boldsymbol{p}_{S}(\boldsymbol{h}_{\lambda}) - \boldsymbol{p}_{S}(\boldsymbol{h}), \tilde{\boldsymbol{u}}_{S})$$

$$= \sum_{i=1}^{n_{\mathcal{E}}} ((h^{i})^{4} - (h^{i}_{\lambda})^{4}) \int_{0}^{\ell^{i}} \mathbf{Q}^{i} \tilde{\mathbf{H}}^{i}(\mathbf{Q}^{i})^{T} \partial_{s} \boldsymbol{\omega}^{i}(\boldsymbol{h}_{\lambda}) \cdot \partial_{s} \tilde{\boldsymbol{\omega}}^{i} ds$$

$$b_{S}(\tilde{\boldsymbol{p}}_{S}, \boldsymbol{u}_{S}(\boldsymbol{h}_{\lambda}) - \boldsymbol{u}_{S}(\boldsymbol{h})) = 0.$$

$$(3.9)$$

This is exactly of the form (3.8) with the right-hand side equal to

$$\langle \boldsymbol{F}_{\lambda}, \tilde{\boldsymbol{u}}_{S} \rangle = \sum_{i=1}^{n_{\mathcal{E}}} ((h_{\lambda}^{i})^{4} - (h^{i})^{4}) \int_{0}^{\ell^{i}} \mathbf{Q}^{i} \tilde{\mathbf{H}}^{i} (\mathbf{Q}^{i})^{T} \partial_{s} \boldsymbol{\omega}^{i} (\boldsymbol{h}_{\lambda}) \cdot \partial_{s} \tilde{\boldsymbol{\omega}}^{i} ds.$$

By the Cauchy-Schwarz inequality, and by the upper bound on the matrix H, we have

$$\begin{aligned} |\langle \boldsymbol{F}_{\lambda}, \tilde{\boldsymbol{u}}_{S} \rangle| &\leq \sum_{i=1}^{n_{\mathcal{E}}} \left| (h_{\lambda}^{i})^{4} - (h^{i})^{4} \right| \|\tilde{\mathbf{H}}^{i}\| \|\partial_{s} \boldsymbol{\omega}^{i}(\boldsymbol{h}_{\lambda})\|_{L^{2}(0, \ell^{i}; \mathbb{R}^{3})} \|\partial_{s} \tilde{\boldsymbol{\omega}}^{i}\|_{L^{2}(0, \ell^{i}; \mathbb{R}^{3})} \\ &\leq C \max_{i=1, \dots, n_{\mathcal{E}}} \left| (h_{\lambda}^{i})^{4} - (h^{i})^{4} \right| \|\tilde{\boldsymbol{u}}_{S}\|_{H^{1}(\mathcal{N}; \mathbb{R}^{6})}, \end{aligned}$$

where, in the last inequality, we have used the uniform boundedness  $\|\boldsymbol{u}_{S}(\boldsymbol{h}_{\lambda})\|_{H^{1}(\mathcal{N};\mathbb{R}^{6})} < M$  discussed above, to estimate the term  $\|\partial_{s}\boldsymbol{\omega}^{i}(\boldsymbol{h}_{\lambda})\|_{L^{2}(0,\ell^{i};\mathbb{R}^{3})}$ . As  $\boldsymbol{h}_{\lambda} \to \boldsymbol{h}$ , we see that the right-hand side of the inequality goes to zero, and so by the second part of Lemma 3.2, we obtain that  $(\boldsymbol{u}_{S}^{\boldsymbol{h}_{\lambda}}, \boldsymbol{p}_{S}^{\boldsymbol{h}_{\lambda}}) = (\boldsymbol{u}_{S}(\boldsymbol{h}_{\lambda}) - \boldsymbol{u}(\boldsymbol{h}), \boldsymbol{p}_{S}(\boldsymbol{h}_{\lambda}) - \boldsymbol{p}(\boldsymbol{h})) \to 0$  in  $H^{1}(\mathcal{N}; \mathbb{R}^{6}) \times L^{2}(\mathcal{N}; \mathbb{R}^{3})$ , as  $\boldsymbol{h}_{\lambda} \to \boldsymbol{h}$ .

Proof of Lemma 3.2. The proof of Lemma 3.2 relies on the following result from [8].

**Theorem 3.3** (Brezzi, Fortin, TM 1.1. [8]). Let V and Q be Hilbert spaces with associated norms  $\|\cdot\|_V$  and  $\|\cdot\|_Q$ . Let the continuous bilinear forms  $k: V \times V \to \mathbb{R}$  and  $b: V \times Q \to \mathbb{R}$  satisfy

$$|k(u, \tilde{u})| \leq A_0 ||u||_V ||\tilde{u}||_V, \quad \forall u, \tilde{u} \in V,$$

$$|b(u, p)| \leq B_0 ||u||_V ||p||_Q, \quad \forall u \in V, p \in Q,$$

$$k(u, u) \geq \alpha_0 ||u||_V^2, \quad \forall u \text{ such that } b(u, p) = 0 \ \forall p \in Q,$$

$$\inf_{p \in Q} \sup_{u \in V} \frac{b(u, p)}{||u||_V ||p||_Q} \geq \beta_0,$$
(3.10)

for some positive constants  $A_0$ ,  $B_0$ ,  $\alpha_0$ ,  $\beta_0$ . Let  $f \in V'$ ,  $g \in Q'$ . Then there exists a unique solution  $(u, p) \in V \times Q$  of

$$k(u, \tilde{u}) + b(\tilde{u}, p) = \langle f, \tilde{u} \rangle_{V', V}, \qquad \forall \tilde{u} \in V,$$
  
$$b(u, \tilde{p}) = \langle g, \tilde{p} \rangle_{Q', Q}, \qquad \forall \tilde{p} \in Q.$$
 (3.11)

Moreover, the solution (u, p) satisfies the bounds

$$||u||_{V} \leq \frac{1}{\alpha_{0}} ||f||'_{V} + \frac{1}{\beta_{0}} \left( \frac{A_{0}}{\alpha_{0}} + 1 \right) ||g||'_{Q},$$

$$||p||_{Q} \leq \frac{1}{\beta_{0}} \left( \frac{A_{0}}{\alpha_{0}} + 1 \right) ||f||'_{V} + \frac{A_{0}}{\beta_{0}^{2}} \left( \frac{A_{0}}{\alpha_{0}} + 1 \right) ||g||'_{Q}.$$
(3.12)

This theorem, as stated above, is in fact a special case of Theorem 1.1. [8] in the sense that the last inequality in (3.10) is more restrictive than the corresponding condition in the original statement of Theorem 1.1. [8]. As a result, the original Theorem 1.1. [8] guarantees uniqueness of the second component p of the solution (u, p) up to a function from the function space  $\{p \in Q : b(\tilde{u}, p) = 0 \ \forall \tilde{u} \in V\}$ . The last inequality from (3.10) as stated in Theorem 3.3 above, implies that this function space is trivial, and so uniqueness is guaranteed in Theorem 3.3.

From this theorem, we see that if we can show that there exist uniform constants  $A_0$ ,  $B_0$ ,  $\alpha_0$ ,  $\beta_0$  such that problems (3.8) satisfy the estimates (3.10) uniformly for all  $\lambda$ , then both claims of Lemma 3.2 follow directly from the estimates (3.12).

We start by noting that the bilinear form  $b_S$  does not depend on  $\lambda$ . Then, Lemma 3.5 in [21] implies the existence of constants  $B_0 > 0$  and  $\beta_0 > 0$  such that the estimates involving  $b_S$  in (3.10) hold.

What is left is to show the continuity and coercivity estimates on  $k_S$ . For this purpose, we recall the definition of the form  $k_S$ :

$$k_S(\boldsymbol{h}_{\lambda})(\boldsymbol{u}_S, \tilde{\boldsymbol{u}}_S) = \sum_{i=1}^{n_{\mathcal{E}}} (h_{\lambda}^i)^4 \int_0^{\ell_i} \mathbf{Q}^i \tilde{\mathbf{H}}^i(\mathbf{Q}^i)^T \partial_s \boldsymbol{\omega}^i \cdot \partial_s \tilde{\boldsymbol{\omega}}^i ds.$$

The continuity estimate now follows directly from the boundedness of the matrix  $\tilde{\mathbf{H}}^i$ . More precisely, if we denote by C > 0 the constant that bounds the matrix norm of  $\tilde{\mathbf{H}}^i$ , and by recalling that for all  $\mathbf{h}_{\lambda} \in W$  we have  $h_{\min} \leq h_{\lambda}^i \leq h_{\max}$ , the Cauchy–Schwarz inequality implies

$$k_{S}(\boldsymbol{h}_{\lambda})(\boldsymbol{u}_{S}, \tilde{\boldsymbol{u}}_{S}) \leq h_{\max}^{4} C \left( \sum_{i=1}^{n_{\mathcal{E}}} \|\partial_{s} \boldsymbol{\omega}^{i}\|_{L^{2}(0,\ell_{i};\mathbb{R}^{3})}^{2} \right)^{1/2} \left( \sum_{i=1}^{n_{\mathcal{E}}} \|\partial_{s} \tilde{\boldsymbol{\omega}}^{i}\|_{L^{2}(0,\ell_{i};\mathbb{R}^{3})}^{2} \right)^{1/2}$$

$$\leq h_{\max}^{4} C \|\boldsymbol{u}_{S}\|_{H^{1}(\mathcal{N};\mathbb{R}^{6})} \|\tilde{\boldsymbol{u}}_{S}\|_{H^{1}(\mathcal{N};\mathbb{R}^{6})}.$$
(3.13)

By choosing the uniform constant  $A_0 = h_{\text{max}}^4 C$ , we have shown continuity of  $k_S$ .

The uniform coercitivity of  $k_S$  follows from the coercivity associated with the matrix  $\tilde{\mathbf{H}}^i$ , and a Poincaré type inequality. More precisely, from Lemma 3.2. [21], we see that there exists a constant  $C_P > 0$ , independent of  $\lambda$ , such that

$$\begin{aligned} \|\boldsymbol{u}_{S}\|_{H^{1}(\mathcal{N};\mathbb{R}^{6})}^{2} &= \sum_{i=1}^{n_{\mathcal{E}}} \left( \|\boldsymbol{u}^{i}\|_{H^{1}(0,\ell_{i};\mathbb{R}^{3})}^{2} + \|\boldsymbol{\omega}^{i}\|_{H^{1}(0,\ell_{i};\mathbb{R}^{3})}^{2} \right) \\ &\leq C_{P} \left( \sum_{i=1}^{n_{\mathcal{E}}} \|\partial_{s}\boldsymbol{u}^{i}\|_{L^{2}(0,\ell_{i};\mathbb{R}^{3})}^{2} + \sum_{i=1}^{n_{\mathcal{E}}} \|\partial_{s}\boldsymbol{\omega}^{i}\|_{L^{2}(0,\ell_{i};\mathbb{R}^{3})}^{2} \right) + \left| \sum_{i=1}^{n_{\mathcal{E}}} \int_{0}^{\ell_{i}} \boldsymbol{u}^{i} ds \right| + \left| \sum_{i=1}^{n_{\mathcal{E}}} \int_{0}^{\ell_{i}} \boldsymbol{\omega}^{i} ds \right| \end{aligned}$$

This is a Poincaré type estimate for the stent problem, obtained in [21]. We further estimate the right-hand side by recalling that this coercivity estimate is done over the space of constraints V, namely for all u such that  $b(u,p) = 0, \forall p \in Q$ , see (3.10), which includes the conditions that make the last two terms on the right-hand side above equal to zero. Therefore, the right-hand side can be further estimated by

$$\leq 2C_{P} \sum_{i=1}^{n_{\mathcal{E}}} \left( \|\partial_{s} \boldsymbol{u}^{i} + \boldsymbol{t}^{i} \times \boldsymbol{\omega}^{i}\|_{L^{2}(0,\ell_{i};\mathbb{R}^{3})}^{2} + \|\boldsymbol{t}^{i} \times \boldsymbol{\omega}^{i}\|_{L^{2}(0,\ell_{i};\mathbb{R}^{3})}^{2} + \|\partial_{s} \boldsymbol{\omega}^{i}\|_{L^{2}(0,\ell_{i};\mathbb{R}^{3})}^{2} \right) \\
\leq \tilde{C} \sum_{i=1}^{n_{\mathcal{E}}} \|\partial_{s} \boldsymbol{\omega}^{i}\|_{L^{2}(0,\ell_{i};\mathbb{R}^{3})}^{2},$$

where we again used that the space V includes the constraint  $\partial_s \mathbf{u}^i + \mathbf{t}^i \times \boldsymbol{\omega}^i = 0$  via  $b(u, p) = 0, \forall p \in Q$ . If we now denote by  $a_0$  the coercivity constant associated with  $\tilde{\mathbf{H}}^i$ , we can further estimate the above inequality as

$$\tilde{C}\sum_{i=1}^{n_{\mathcal{E}}} \|\partial_s \boldsymbol{\omega}^i\|_{L^2(0,\ell_i;\mathbb{R}^3)}^2 \leq \tilde{C}\frac{a_0}{h_{\min}^4} \sum_{i=1}^{n_{\mathcal{E}}} (h_{\lambda}^i)^4 \int_0^{\ell_i} \mathbf{Q}^i \tilde{\mathbf{H}}^i (\mathbf{Q}^i)^T \partial_s \boldsymbol{\omega}^i \cdot \partial_s \tilde{\boldsymbol{\omega}}^i ds \leq \frac{\tilde{C}a_0}{h_{\min}^4} k_S(\boldsymbol{h}_{\lambda})(\boldsymbol{u}_S, \tilde{\boldsymbol{u}}_S),$$

which completes the proof of coercivity of k.

The statements of Lemma 3.2 then follow directly from Theorem 3.3.

We have now completed the proof of continuity of  $h \mapsto \tilde{J}(h)$  and are ready to state the main result of this subsection.

**Theorem 3.4.** The constrained minimization problem (3.4) has a solution.

*Proof.* The set W is a closed and bounded subset of  $\mathbb{R}^{n_{\mathcal{E}}}$ , and is therefore compact. From Theorem 3.1 we obtained that  $\tilde{J}$  is continuous on W. Therefore,  $\tilde{J}$  possesses extrema on W.  $\square$ 

### 3.1.2 The iteration algorithm

We present an iteration algorithm for solving the optimization problem (3.4). We begin with a given h, and look for a  $g \in \mathbb{R}^{n_{\mathcal{E}}}$  such that

$$\tilde{J}(\boldsymbol{h}+\boldsymbol{g}) \leq \tilde{J}(\boldsymbol{h}).$$

Assuming that  $\tilde{J}$  admits the Taylor series expansion around h, we obtain:

$$\tilde{J}(\boldsymbol{h}) + d_{\boldsymbol{h}}\tilde{J}(\boldsymbol{h})\boldsymbol{g} + o(\boldsymbol{g}) \leq \tilde{J}(\boldsymbol{h}).$$

Here  $d_h \tilde{J}(h)g$  is the Gateaux derivative of the functional  $\tilde{J}$  in the direction of g. Thus, in order to decrease the value of the cost function in each step, we look for a g such that

$$d_{\mathbf{h}}\tilde{J}(\mathbf{h})\mathbf{g} \le 0. \tag{3.14}$$

This leads to a gradient based method.

More precisely, from the definition of the Gateaux derivative, we calculate  $d_h \tilde{J}(h)g$  as follows:

$$d_{h}\tilde{J}(h)g = \lim_{\lambda \to 0} \frac{\tilde{J}(h + \lambda g) - \tilde{J}(h)}{\lambda} = \lim_{\lambda \to 0} \frac{\sum_{i=1}^{n_{\mathcal{E}}} \int_{0}^{\ell^{i}} f^{i} \cdot u^{i}(h + \lambda g) ds - \sum_{i=1}^{n_{\mathcal{E}}} \int_{0}^{\ell^{i}} f^{i} \cdot u^{i}(h) ds}{\lambda}$$
$$= \lim_{\lambda \to 0} \sum_{i=1}^{n_{\mathcal{E}}} \int_{0}^{\ell^{i}} f^{i} \cdot \frac{u^{i}(h + \lambda g) - u^{i}(h)}{\lambda} ds = \sum_{i=1}^{n_{\mathcal{E}}} \int_{0}^{\ell^{i}} f^{i} \cdot d_{h}u^{i}(h) g ds.$$

Therefore,

$$d_{\mathbf{h}}\tilde{J}(\mathbf{h})\mathbf{g} = \sum_{i=1}^{n_{\mathcal{E}}} \int_{0}^{\ell^{i}} \mathbf{f}^{i} \cdot d_{\mathbf{h}} \mathbf{u}^{i}(\mathbf{h}) \mathbf{g} ds.$$
(3.15)

What is left is to "calculate"  $d_{\mathbf{h}}\mathbf{u}^{i}(\mathbf{h})\mathbf{g}$ . More precisely, we will derive a system of equations satisfied by  $d_{\mathbf{h}}\mathbf{u}^{i}(\mathbf{h})\mathbf{g}$ . This system is obtained directly from the system (3.9) for  $\mathbf{h}_{\lambda} = \mathbf{h} + \lambda \mathbf{g}$  after dividing the first equation in (3.9) by  $\lambda$  and after taking the limit  $\lambda \to 0$ , to obtain

$$\begin{aligned} k_S(\boldsymbol{h})(d_{\boldsymbol{h}}\boldsymbol{u}_S(\boldsymbol{h})\boldsymbol{g},\tilde{\boldsymbol{u}}_S) + b_S(d_{\boldsymbol{h}}\boldsymbol{p}_S(\boldsymbol{h})\boldsymbol{g},\tilde{\boldsymbol{u}}_S) \\ &= -(d_{\boldsymbol{h}}k_S(\boldsymbol{h})\boldsymbol{g})(\boldsymbol{u}_S(\boldsymbol{h}),\tilde{\boldsymbol{u}}_S) := -\sum_{i=1}^{n_{\mathcal{E}}} 4(h^i)^3 g^i \int_0^{\ell^i} \mathbf{Q}^i \tilde{\mathbf{H}}^i(\mathbf{Q}^i)^T \partial_s \boldsymbol{\omega}^i(\boldsymbol{h}) \cdot \partial_s \tilde{\boldsymbol{\omega}}^i ds. \end{aligned}$$

From the definition of the bilinear form  $k_S$ , we see that the right-hand side can be expressed as  $k_S(\mathbf{h}_{\mathbf{g}})(\mathbf{u}_S(\mathbf{h}), \tilde{\mathbf{u}}_S)$ , where  $(\mathbf{h}_{\mathbf{g}})^i = -4(h^i)^3 g^i, i = 1, \dots, n_{\mathcal{E}}$ . Therefore,

$$-(d_{\boldsymbol{h}}k_{S}(\boldsymbol{h})\boldsymbol{g})(\boldsymbol{u}_{S}(\boldsymbol{h}), \tilde{\boldsymbol{u}}_{S}) = k_{S}(\boldsymbol{h}_{\boldsymbol{g}})(\boldsymbol{u}_{S}(\boldsymbol{h}), \tilde{\boldsymbol{u}}_{S}), \text{ where } (\boldsymbol{h}_{\boldsymbol{g}})^{i} = -4(h^{i})^{3}g^{i}, i = 1, \dots, n_{\mathcal{E}}.$$

Thus, the first equation satisfied by  $d_h u_S(h)g$  is

$$k_S(\boldsymbol{h})(d_{\boldsymbol{h}}\boldsymbol{u}_S(\boldsymbol{h})\boldsymbol{g},\tilde{\boldsymbol{u}}_S) + b_S(d_{\boldsymbol{h}}\boldsymbol{p}_S(\boldsymbol{h})\boldsymbol{g},\tilde{\boldsymbol{u}}_S) = k_S(\boldsymbol{h}_{\boldsymbol{g}})(\boldsymbol{u}_S(\boldsymbol{h}),\tilde{\boldsymbol{u}}_S), \quad \tilde{\boldsymbol{u}}_S \in V_S.$$

The second equation satisfied by  $d_{\mathbf{h}}\mathbf{u}_{S}(\mathbf{h})\mathbf{g}$  follows directly from the second equation in (3.9) with  $\mathbf{h}_{\lambda} = \mathbf{h} + \lambda \mathbf{g}$ . Namely, since  $b_{S}$  does not depend on  $\mathbf{h}$ , we easily obtain

$$b_S\left(\tilde{\boldsymbol{p}}_S, \frac{\boldsymbol{u}_S(\boldsymbol{h} + \lambda \boldsymbol{g}) - \boldsymbol{u}_S(\boldsymbol{h})}{\lambda}\right) = 0 \implies b_S(\tilde{\boldsymbol{p}}_S, d_{\boldsymbol{h}}\boldsymbol{u}_S(\boldsymbol{h})\boldsymbol{g}) = 0.$$

Therefore,  $(d_h u_S(h)g, d_h p_S(h)g) \in V_S \times Q_S$  satisfy the following system of equations:

$$k_{S}(\boldsymbol{h})(d_{\boldsymbol{h}}\boldsymbol{u}_{S}(\boldsymbol{h})\boldsymbol{g},\tilde{\boldsymbol{u}}_{S}) + b_{S}(d_{\boldsymbol{h}}\boldsymbol{p}_{S}(\boldsymbol{h})\boldsymbol{g},\tilde{\boldsymbol{u}}_{S}) = k_{S}(\boldsymbol{h}_{\boldsymbol{g}})(\boldsymbol{u}_{S}(\boldsymbol{h}),\tilde{\boldsymbol{u}}_{S}), \quad \forall \tilde{\boldsymbol{u}}_{S} \in V_{S},$$

$$b_{S}(\tilde{\boldsymbol{p}}_{S},d_{\boldsymbol{h}}\boldsymbol{u}_{S}(\boldsymbol{h})) = 0, \quad \forall \tilde{\boldsymbol{p}}_{S} \in Q_{S}.$$

$$(3.16)$$

This formal derivation is now rigorously justified by the following result.

**Theorem 3.5.** Let  $(\mathbf{u}_S(\mathbf{h}), \mathbf{p}_S(\mathbf{h}))$  be a family (parameterized by  $\mathbf{h}$ ) of unique solutions of (3.2). Then, the following limits exist:

$$d_{\boldsymbol{h}}\boldsymbol{u}_{S}(\boldsymbol{h})\boldsymbol{g}:=\lim_{\lambda\to 0}\frac{1}{\lambda}(\boldsymbol{u}_{S}(\boldsymbol{h}+\lambda\boldsymbol{g})-\boldsymbol{u}_{S}(\boldsymbol{h})), \qquad d_{\boldsymbol{h}}\boldsymbol{p}_{S}(\boldsymbol{h})\boldsymbol{g}:=\lim_{\lambda\to 0}\frac{1}{\lambda}(\boldsymbol{p}_{S}(\boldsymbol{h}+\lambda\boldsymbol{g})-\boldsymbol{p}_{S}(\boldsymbol{h})).$$

Furthermore, the limits above are unique solutions of (3.16).

*Proof.* For each fixed h, consider the system (3.16), and denote by  $(d_h u_S(h)g, d_h p_S(h)g)$  its unique solution. Notice that system (3.16) is of the form discussed in Theorem 3.3, which guarantees the existence of a unique solution. We now show that this solution is, in fact, the limit as  $\lambda \to 0$  of  $(\frac{1}{\lambda}(u_S(h + \lambda g) - u_S(h)), \frac{1}{\lambda}(p_S(h + \lambda g) - p_S(h)))$ . For this purpose, for each  $\lambda$  define

$$oxed{(oldsymbol{u}_S^{\lambda},oldsymbol{p}_S^{\lambda})} := rac{1}{\lambda}(oldsymbol{u}_S(oldsymbol{h}+\lambdaoldsymbol{g}) - oldsymbol{u}_S(oldsymbol{h}), oldsymbol{p}_S(oldsymbol{h}+\lambdaoldsymbol{g}) - oldsymbol{p}_S(oldsymbol{h})).$$

We first see that functions  $(\boldsymbol{u}_{S}^{\lambda}, \boldsymbol{p}_{S}^{\lambda})$  are solutions of system (3.8), with

$$\langle \boldsymbol{F}_{\lambda}, \tilde{\boldsymbol{u}}_{S} \rangle = \sum_{i=1}^{n_{\mathcal{E}}} \frac{1}{\lambda} ((h^{i} + \lambda g^{i})^{4} - (h^{i})^{4}) \int_{0}^{\ell^{i}} \mathbf{Q}^{i} \tilde{\mathbf{H}}^{i} (\mathbf{Q}^{i})^{T} \partial_{s} \boldsymbol{\omega}^{i} (\boldsymbol{h} + \lambda \boldsymbol{g}) \cdot \partial_{s} \tilde{\boldsymbol{\omega}}^{i} ds.$$

Now we focus on the factor multiplying the integral in the source term  $\langle \boldsymbol{F}_{\lambda}, \tilde{\boldsymbol{u}}_{S} \rangle$ , and introduce the functions

$$\phi_{\lambda}(t) := \frac{1}{\lambda}((t + \lambda c)^4 - t^4) = 4t^3c + 6t^2\lambda c^2 + 4t\lambda^2c^3 + \lambda^3c^4,$$

where c > 0 is arbitrary. We see that  $\phi_{\lambda}(t)$  are uniformly (in  $\lambda$ ) bounded on  $t \in [h_{\min}, h_{\max}]$  for small  $\lambda$ , and the functions  $\phi_{\lambda}$  converge uniformly to  $\phi_{0}(t) = 4t^{3}c$ , as  $\lambda \to 0$ . Thus the family  $\mathbf{F}_{\lambda}$  is uniformly bounded, since we showed in the proof of Lemma 3.2 that  $(\mathbf{u}_{S}(\mathbf{h} + \lambda \mathbf{g}) - \mathbf{u}(\mathbf{h}), \mathbf{p}_{S}(\mathbf{h} + \lambda \mathbf{g}) - \mathbf{p}(\mathbf{h})) \to 0$  in  $H^{1}(\mathcal{N}; \mathbb{R}^{6}) \times L^{2}(\mathcal{N}; \mathbb{R}^{3})$ , as  $\lambda \to 0$ , which implies that the integrand is uniformly bounded as well. Therefore, by the first statement of Lemma 3.2, functions  $(\mathbf{u}_{S}^{\lambda}, \mathbf{p}_{S}^{\lambda})$  are uniformly bounded in  $H^{1}(\mathcal{N}; \mathbb{R}^{6}) \times L^{2}(\mathcal{N}; \mathbb{R}^{3})$ .

Finally, we consider the functions

$$(\boldsymbol{u}_S^{\lambda}-d_{\boldsymbol{h}}\boldsymbol{u}_S(\boldsymbol{h})\boldsymbol{g},\boldsymbol{p}_S^{\lambda}-d_{\boldsymbol{h}}\boldsymbol{p}_S(\boldsymbol{h})\boldsymbol{g})$$

and notice that they are also solutions of (3.8), with

$$\langle \boldsymbol{F}_{\lambda}, \tilde{\boldsymbol{u}}_{S} \rangle = \sum_{i=1}^{n_{\mathcal{E}}} \left( \frac{(h^{i} + \lambda g^{i})^{4}) - (h^{i})^{4}}{\lambda} - 4(h^{i})^{3} g^{i} \right) \int_{0}^{\ell^{i}} \mathbf{Q}^{i} \tilde{\mathbf{H}}^{i}(\mathbf{Q}^{i})^{T} \partial_{s} \boldsymbol{\omega}^{i} (\boldsymbol{h} + \lambda \boldsymbol{g}) \cdot \partial_{s} \tilde{\boldsymbol{\omega}}^{i} ds,$$

which converges to zero by a similar argument as above. The second statement of Lemma 3.2 now implies that the sequence  $(\boldsymbol{u}_S^{\lambda} - d_{\boldsymbol{h}}\boldsymbol{u}_S(\boldsymbol{h})\boldsymbol{g}, \boldsymbol{p}_S^{\lambda} - d_{\boldsymbol{h}}\boldsymbol{p}_S(\boldsymbol{h})\boldsymbol{g}) \to (0,0)$  in  $H^1(\mathcal{N}; \mathbb{R}^6) \times L^2(\mathcal{N}; \mathbb{R}^3)$ , which completes the proof.

**Remark 3.1.** Since  $d_{\mathbf{h}}\mathbf{u}_{S}(\mathbf{h})\mathbf{g}$  is the solution of (3.16) which is of the form (3.7) we can apply similar arguments from the proof of Theorem 3.1 to conclude that  $d_{\mathbf{h}}\mathbf{u}_{S}(\mathbf{h})\mathbf{g}$  is continuous with respect to  $\mathbf{h}$ . This also implies the Fréchet differentiability of  $\tilde{J}$  and that  $\tilde{J}$  is of class  $C^{1}$ .

Now that we have determined  $d_{\mathbf{h}}\mathbf{u}^{i}(\mathbf{h})\mathbf{g}$ , we return to the expression (3.15) which specified the relationship between  $d_{\mathbf{h}}\mathbf{u}^{i}(\mathbf{h})\mathbf{g}$  and  $d_{\mathbf{h}}\tilde{J}(\mathbf{h})\mathbf{g}$  to further simplify the calculation of  $d_{\mathbf{h}}\tilde{J}(\mathbf{h})\mathbf{g}$ . More precisely, using (3.16) we get:

$$d_{\mathbf{h}}\tilde{J}(\mathbf{h})\mathbf{g} = \sum_{i=1}^{n_{\mathcal{E}}} \int_{0}^{\ell^{i}} \mathbf{f}^{i} \cdot d_{\mathbf{h}} \mathbf{u}^{i}(\mathbf{h}) \mathbf{g} ds = l_{S}(d_{\mathbf{h}} \mathbf{u}_{S}(\mathbf{h}) \mathbf{g})$$

$$= k_{S}(\mathbf{h})(\mathbf{u}_{S}(\mathbf{h}), d_{\mathbf{h}} \mathbf{u}_{S}(\mathbf{h}) \mathbf{g}) + b_{S}(\mathbf{p}_{S}(\mathbf{h}), d_{\mathbf{h}} \mathbf{u}_{S}(\mathbf{h}) \mathbf{g})$$

$$= k_{S}(\mathbf{h})(\mathbf{u}_{S}(\mathbf{h}), d_{\mathbf{h}} \mathbf{u}_{S}(\mathbf{h}) \mathbf{g}) = k_{S}(\mathbf{h}_{\mathbf{g}})(\mathbf{u}_{S}(\mathbf{h}), \mathbf{u}_{S}(\mathbf{h})).$$

$$(3.17)$$

From this equation we conclude that the minimization problem for the functional  $\tilde{J}$ , described by the inequality (3.14), reduces to finding a g such that

$$\begin{cases}
-\sum_{i=1}^{n_{\mathcal{E}}} 4(h^{i})^{3} g^{i} \int_{0}^{\ell^{i}} \mathbf{Q}^{i} \tilde{\mathbf{H}}^{i}(\mathbf{Q}^{i})^{T} \partial_{s} \boldsymbol{\omega}^{i}(\boldsymbol{h}) \cdot \partial_{s} \boldsymbol{\omega}^{i}(\boldsymbol{h}) ds = k_{S}(\boldsymbol{h}_{g})(\boldsymbol{u}_{S}(\boldsymbol{h}), \boldsymbol{u}_{S}(\boldsymbol{h})) \leq 0, \\
\text{where } \boldsymbol{u}_{S}(\boldsymbol{h}) \text{ solves (3.2) for a given } \boldsymbol{h}.
\end{cases}$$
(3.18)

Since the form  $\int_0^{\ell^i} \mathbf{Q}^i \tilde{\mathbf{H}}^i(\mathbf{Q}^i)^T \partial_s \boldsymbol{\omega}^i(\boldsymbol{h}) \cdot \partial_s \boldsymbol{\omega}^i(\boldsymbol{h}) ds$  is positive definite, this implies that any  $\boldsymbol{g}$  consisting of nonnegative components  $g^i$ , will decrease the value of the functional  $\tilde{J}$ . However, the gradient descent method is obtained for the choice

$$g^{i} := (h^{i})^{3} \int_{0}^{\ell^{i}} \mathbf{Q}^{i} \tilde{\mathbf{H}}^{i} (\mathbf{Q}^{i})^{T} \partial_{s} \boldsymbol{\omega}^{i} (\boldsymbol{h}) \cdot \partial_{s} \boldsymbol{\omega}^{i} (\boldsymbol{h}) ds, \tag{3.19}$$

(3.20)

for  $i = 1, \ldots, n_{\mathcal{E}}$ .

Finally, one has to take into account the conditions on the minimal and maximal thickness and the total volume constraint. This can be done as in [1, 2] by constructing a projection operator  $P_W$  onto the set of constraints W, defined in (3.5), and using an iteration procedure

$$\boldsymbol{h}_{n+1} = P_W(\boldsymbol{h}_n + \alpha \boldsymbol{g}), \quad n > 0$$

until convergence. Here  $\alpha > 0$  is the descent step,  $P_W$  is the projection operator onto the closed convex set W, and the derivative  $d_h \tilde{J}(h)g$  is calculated in (3.17).

The following is the resulting stent constrained optimization algorithm:

#### Initialization

prescribe initial  $h^0$  compute the solution  $(\boldsymbol{u}_S(\boldsymbol{h}^0), \boldsymbol{p}_S(\boldsymbol{h}^0))$  of (3.2) compute  $\tilde{J}(\boldsymbol{h}^0)$ 

#### Iterations

compute  $\mathbf{g}$  using (3.19) update  $\mathbf{h} = \mathbf{h} + \alpha \mathbf{g}$  for appropriate  $\alpha$ calculate the projection  $P_W$  onto the constraints set Wcompute the solution  $(\mathbf{u}_S(\mathbf{h}), \mathbf{p}_S(\mathbf{h}))$  of (3.2) compute  $\tilde{J}(\mathbf{h})$ 

# 3.2 Rectangular cross-sections: Perturbations with respect to $w_i$ .

In this case the cross-sections are rectangles with sides h and  $w_i$  corresponding to the thickness and width, respectively, of the ith strut. Numerically, each strut will be subdivided into n substruts, in which case  $w_i$  will be associated with each sub-strut. This effectively means that the width of each strut at the continuous level will be a function of s. See, e.g., Fig. 6 right, where the width of a single stent strut is shown versus axis of symmetry of the stent. Since stents are often cut out of a metallic tube of a certain fixed thickness, we are assuming that the thickness h of all the stent struts is constant. The rectangles are positioned in such a way that the thickness is aligned with the direction of the normal vector  $n^i$  to the middle line of the curved rod, while

the width is aligned with the binormal vector  $b^i$ , see Fig. 3. The normal vector to the middle line is also normal to the cylinder describing the arterial wall. In this case we have:

$$I_i^{23} = 0, \qquad I_{33}^i = \int_{-h/2}^{h/2} \int_{-w_i/2}^{w_i/2} x_3^2 dx_2 dx_3 = \frac{h w_i^3}{12}, \qquad I_{22}^i = \int_{-h/2}^{h/2} \int_{-w_i/2}^{w_i/2} x_2^2 dx_2 dx_3 = \frac{h^3 w_i}{12}.$$

For torsional rigidity we use the series (3.1), where w is replaced by  $w_i$ , and denote the resulting function of tube thickness h and strut width  $w_i$  by  $K(h, w_i)$ . In the numerical simulations, we use the first seven terms in the series for  $K(h, w_i)$  as an approximation. With this notation, we have:

$$\mathbf{H}^{i}(\boldsymbol{w}) = \begin{bmatrix} \mu^{i} K(h, w_{i}) & 0 & 0\\ 0 & E^{i} \frac{h w_{i}^{3}}{12} & 0\\ 0 & 0 & E^{i} \frac{h^{3} w_{i}}{12} \end{bmatrix}, \text{ where } K(h, w_{i}) \text{ is given by (3.1)}.$$

After using the same arguments as in the previous section, we conclude that:

$$d_{\boldsymbol{w}}\tilde{J}(\boldsymbol{w})\boldsymbol{g} = k_{S}(\boldsymbol{w})(\boldsymbol{u}_{S}(\boldsymbol{w}), d_{\boldsymbol{w}}\boldsymbol{u}_{S}(\boldsymbol{w})\boldsymbol{g}) = -d_{\boldsymbol{w}}k_{S}(\boldsymbol{w})\boldsymbol{g}(\boldsymbol{u}_{S}(\boldsymbol{w}), \boldsymbol{u}_{S}(\boldsymbol{w})),$$

where  $d_{\boldsymbol{w}}k_{S}(\boldsymbol{w})\boldsymbol{g}$  is given by

$$(d_{\boldsymbol{w}}k_{S}(\boldsymbol{w})\boldsymbol{g})(\boldsymbol{\omega}^{i},\tilde{\boldsymbol{\omega}}^{i}) = \sum_{i=1}^{n_{\mathcal{E}}} \int_{0}^{\ell^{i}} \mathbf{Q}^{i}(d_{\boldsymbol{w}}\mathbf{H}^{i}(\boldsymbol{w})\boldsymbol{g})(\mathbf{Q}^{i})^{T} \partial_{s}\boldsymbol{\omega}^{i} \cdot \partial_{s}\tilde{\boldsymbol{\omega}}^{i}ds.$$

It is easy to compute

$$d_{\mathbf{w}}\mathbf{H}^{i}(\mathbf{w})\mathbf{g} = \frac{d}{d\lambda}\mathbf{H}^{i}(\mathbf{w} + \lambda \mathbf{g})|_{\lambda=0} = \begin{bmatrix} \mu^{i} \frac{\partial K(h, w_{i})}{\partial w_{i}} g_{i} & 0 & 0\\ 0 & E^{i} \frac{3hw_{i}^{2}g_{i}}{12} & 0\\ 0 & 0 & E^{i} \frac{h^{3}g_{i}}{12} \end{bmatrix}$$
$$= \begin{bmatrix} \mu^{i} \frac{\partial K(h, w_{i})}{\partial w_{i}} & 0 & 0\\ 0 & E^{i} \frac{3hw_{i}^{2}}{12} & 0\\ 0 & 0 & E^{i} \frac{h^{3}}{12} \end{bmatrix} g_{i} =: \hat{\mathbf{H}}^{i}(\mathbf{w})g_{i}.$$

Thus

$$d_{\boldsymbol{w}}\tilde{J}(\boldsymbol{w})\boldsymbol{g} = -\sum_{i=1}^{n_{\mathcal{E}}} g_i \int_0^{\ell^i} \mathbf{Q}^i \hat{\mathbf{H}}^i(\boldsymbol{w}) (\mathbf{Q}^i)^T \partial_s \boldsymbol{\omega}^i \cdot \partial_s \tilde{\boldsymbol{\omega}}^i ds.$$
(3.21)

Therefore, the gradient descent direction is given by the vector g with components

$$g_i = \int_0^{\ell^i} \mathbf{Q}^i \hat{\mathbf{H}}^i(\mathbf{w}) (\mathbf{Q}^i)^T \partial_s \boldsymbol{\omega}^i(\mathbf{w}) \cdot \partial_s \boldsymbol{\omega}^i(\mathbf{w}) ds, \qquad i = 1, \dots, n_{\mathcal{E}},$$
(3.22)

where  $(\boldsymbol{u}_S(\boldsymbol{w}), \boldsymbol{p}_S(\boldsymbol{w}))$  is the unique solution of (3.2), and  $\boldsymbol{u}_S(\boldsymbol{w}) = (\boldsymbol{y}^1(\boldsymbol{w}), \dots, \boldsymbol{y}^{n_{\mathcal{E}}}(\boldsymbol{w}))$ , where  $\boldsymbol{y}^i(\boldsymbol{w}) = (\boldsymbol{u}^i(\boldsymbol{w}), \boldsymbol{\omega}^i(\boldsymbol{w}))$ .

The constrained stent optimization algorithm looks the same as the boxed algorithm at the end of Section 3.1, except that g now is calculated using (3.22). Furthermore the existence of the minima of the cost functional also follows in the same way, now using the fact that matrices  $\hat{\mathbf{H}}^i$  depend smoothly on w.

### 3.3 Rectangular cross-sections: perturbations with respect to both $w_i$ and h.

In this subsection the optimization is performed with respect to two parameters, the width and the thickness of each stent strut, where the thickness h is the same for all stent struts. This is

motivated by the fact that balloon expandable stents are typically cut out of a single slotted tube of thickness h. As a result, the steepest descent vector  $\overline{g}$  now has two components:  $\overline{g} := (g_0, g)$ , and the matrix  $\mathbf{H}^i$  describing the elastic properties of the ith strut is now denoted by:

$$\mathbf{H}^{i}(h, \boldsymbol{w}) = \begin{bmatrix} \mu^{i} K(h, w_{i}) & 0 & 0\\ 0 & E^{i} \frac{h w_{i}^{3}}{12} & 0\\ 0 & 0 & E^{i} \frac{h^{3} w_{i}}{12} \end{bmatrix}, \text{ where } K(h, w_{i}) \text{ is given by (3.1)}.$$

To shorten the notation we also introduce the notation  $\overline{\boldsymbol{w}} := (h, \boldsymbol{w})$ . By repeating the arguments from the previous sections, we obtain the following expression for  $d_{\overline{\boldsymbol{w}}} \tilde{J}(\overline{\boldsymbol{w}}) \overline{\boldsymbol{g}} := (d_h \tilde{J}(\overline{\boldsymbol{w}}) \boldsymbol{g}, d_{\boldsymbol{w}} \tilde{J}(\overline{\boldsymbol{w}}) g_0)$ :

$$d_{\overline{\boldsymbol{w}}}\widetilde{J}(\overline{\boldsymbol{w}})\overline{\boldsymbol{g}} = k_S(\overline{\boldsymbol{w}})(\boldsymbol{u}_S(\overline{\boldsymbol{w}}), d_{\overline{\boldsymbol{w}}}\boldsymbol{u}_S(\overline{\boldsymbol{w}})\overline{\boldsymbol{g}}) = -d_{\overline{\boldsymbol{w}}}k_S(\overline{\boldsymbol{w}})\overline{\boldsymbol{g}}(\boldsymbol{u}_S(\boldsymbol{w}), \boldsymbol{u}_S(\boldsymbol{w})),$$

where  $d_{\overline{\boldsymbol{w}}}k_S(\overline{\boldsymbol{w}})\overline{\boldsymbol{g}}$  is given by

$$(d_{\overline{\boldsymbol{w}}}k_{S}(\overline{\boldsymbol{w}})\overline{\boldsymbol{g}})(\boldsymbol{\omega}^{i}, \tilde{\boldsymbol{\omega}}^{i}) = \sum_{i=1}^{n_{\mathcal{E}}} \int_{0}^{\ell^{i}} \mathbf{Q}^{i} (d_{h}\mathbf{H}^{i}(\overline{\boldsymbol{w}})g_{0})(\mathbf{Q}^{i})^{T} \partial_{s} \boldsymbol{\omega}^{i} \cdot \partial_{s} \tilde{\boldsymbol{\omega}}^{i} ds$$
$$+ \sum_{i=1}^{n_{\mathcal{E}}} \int_{0}^{\ell^{i}} \mathbf{Q}^{i} (d_{\boldsymbol{w}}\mathbf{H}^{i}(\overline{\boldsymbol{w}})\boldsymbol{g})(\mathbf{Q}^{i})^{T} \partial_{s} \boldsymbol{\omega}^{i} \cdot \partial_{s} \tilde{\boldsymbol{\omega}}^{i} ds.$$

As before

$$d_{\boldsymbol{w}}\mathbf{H}^{i}(\overline{\boldsymbol{w}})\boldsymbol{g} = \begin{bmatrix} \mu^{i} \frac{\partial K(h, w_{i})}{\partial w_{i}} & 0 & 0\\ 0 & E^{i} \frac{3hw_{i}^{2}}{12} & 0\\ 0 & 0 & E^{i} \frac{h^{3}}{12} \end{bmatrix} g_{i} =: \hat{\mathbf{H}}^{i}(\overline{\boldsymbol{w}})g_{i},$$

while

$$d_{h}\mathbf{H}^{i}(\overline{\boldsymbol{w}})g_{0} = \begin{bmatrix} \mu^{i} \frac{\partial K(h,w_{i})}{\partial h} & 0 & 0\\ 0 & E^{i} \frac{w_{i}^{3}}{12} & 0\\ 0 & 0 & E^{i} \frac{3h^{2}w_{i}}{12} \end{bmatrix} g_{0} =: \hat{\mathbf{H}}^{0}(\overline{\boldsymbol{w}})g_{0}.$$

Therefore the gradient descent direction is given by the vector  $\mathbf{g} = (g_0, \mathbf{g}) = (g_0, g_1, \dots, g_{n_{\mathcal{E}}})$  with components

$$g_{0} = \sum_{i=1}^{n_{\mathcal{E}}} \int_{0}^{\ell^{i}} \mathbf{Q}^{i} \hat{\mathbf{H}}^{0}(\overline{\boldsymbol{w}}) (\mathbf{Q}^{i})^{T} \partial_{s} \boldsymbol{\omega}^{i}(\overline{\boldsymbol{w}}) \cdot \partial_{s} \tilde{\boldsymbol{\omega}}^{i}(\overline{\boldsymbol{w}}) ds,$$

$$g_{i} = \int_{0}^{\ell^{i}} \mathbf{Q}^{i} \hat{\mathbf{H}}^{i}(\overline{\boldsymbol{w}}) (\mathbf{Q}^{i})^{T} \partial_{s} \boldsymbol{\omega}^{i}(\overline{\boldsymbol{w}}) \cdot \partial_{s} \boldsymbol{\omega}^{i}(\overline{\boldsymbol{w}}) ds, \qquad i = 1, \dots, n_{\mathcal{E}},$$

where  $(\boldsymbol{u}_S(\overline{\boldsymbol{w}}), \boldsymbol{p}_S(\overline{\boldsymbol{w}}))$  is the unique solution of (3.2) and  $\boldsymbol{u}_S(\overline{\boldsymbol{w}}) = (\boldsymbol{y}^1(\overline{\boldsymbol{w}}), \dots, \boldsymbol{y}^{n_{\mathcal{E}}}(\overline{\boldsymbol{w}}))$ , where  $\boldsymbol{y}^i(\overline{\boldsymbol{w}}) = (\boldsymbol{u}^i(\overline{\boldsymbol{w}}), \boldsymbol{\omega}^i(\overline{\boldsymbol{w}}))$ .

# 4 The Numerical Method

The stent optimization problems considered in this work are all solved iteratively, with the iteration procedures described in Section 3. A summary of the optimization algorithms is given in (3.20). An important feature of this algorithm is that it is very fast, since in each iteration only one solution of the stent problem has to be solved. One does not need to find the derivative of the cost function, nor the derivatives of the solutions with respect to the optimization parameters, but rather only solve a problem like (3.18), which requires one solution of the stent problem itself. In fact, we performed a comparison with a genetic algorithm implemented in Matlab, see Sec. 6, and showed that not only is our algorithm faster, but the optimal solution of our algorithm has the value of its minimum smaller than that obtained by the genetic algorithm, indicating higher

accuracy of the solution. The stent problem is solved by a FEM method applied to the mixed formulation (2.12). The approach is to first subdivide each edge (stent strut) into subintervals along the middle line of each stent strut. Each subinterval is then treated as a "strut" itself in the sense that the finite elements at the nodes, corresponding to each subinterval, have to satisfy the coupling conditions at each node (continuity of displacement and infinitesimal rotation, and balance of forces and moments). Namely, they belong to the space  $V_S = H^1(\mathcal{N}, \mathbb{R}^6)$  for  $(\boldsymbol{u}_S, \boldsymbol{\omega}_S)$ defined on this "new" stent with an increased number of stent struts. This way we keep the discretized structure unchanged at the expense of changing its description, i.e., the number of vertices, the number of edges, and the split parameterizations. The problem remains given by the equations of the same form (2.12), defined on the associated function space. For the finite dimensional approximations of displacement u and of infinitesimal rotation  $\omega$ , we use piecewise polynomials of order 2, while for the finite dimensional approximation of the contact force  $p_S$ , which is the Lagrange multiplier in the problem, we use piecewise polynomials of order 1. In order for the piecewise polynomials of order 2, approximating  $(u_S, \omega_S)$ , to belong to the space  $V_S = H^1(\mathcal{N}, \mathbb{R}^6)$ , we additionally assume that they are globally continuous (continuous at vertices), while for the first order polynomials approximating  $p_S$  this is not required since they belong to  $L^2(\mathcal{N}, \mathbb{R}^3)$ . It was proved in [22] that this particular approach leads to a convergent approximation of the solution  $(\boldsymbol{u}_S, \boldsymbol{\omega}_S) \in V_S$ .

In the simulations below, the size of the spatial discretization is n=40 for all the stents except for Cypher for which we used n=10 discretization points for non-sinusoidal stent struts in the finest mesh.

# 5 Numerical Results

We show numerical result of optimal design of the following three stents: the Zig-Zag stent (see Fig. 5), the Palmaz6 stent (see Fig. 19), and the Cypher stent (see Fig. 21). We design stents with minimal compliance by changing their struts' width w, and slotted tube thickness h. To avoid having solutions which have infinite strut thickness, we optimize the stents under the constraint that the total volume of struts is kept constant, i.e., the total material used to produce an optimal stent is fixed. We start the optimization process by an initial configuration in which the thickness and width of the stent struts is uniform for all struts in one stent, and it is equal to  $h_0 = 10^{-4}$ m, which is a typical thickness in stent manufacturing. The total volume is then calculated by multiplying  $h_0^2$  by the total length of stent struts. We also fix the minimal and maximal possible thickness to be  $h_{\min} = 10^{-5}m$ ,  $h_{\max} = 10^{-3}m$ . The boundary conditions used in the simulations correspond to the pressure loading applied to the interior stent surface. See Fig. 4. The remaining boundary (stent surface) is force free. This gives rise to a pure

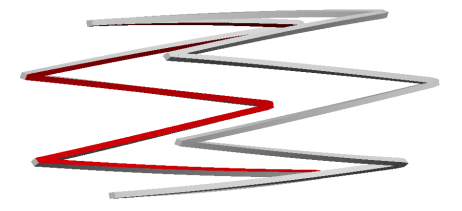


Figure 4: Pure traction boundary conditions: uniform pressure load is applied on the interior stent surface shown in red, and stress free on the rest. Additionally, zero total translation and zero total rotation are prescribed.

traction problem for which the solutions are unique up to translation and rotation. To ensure uniqueness of the solution, zero total translation and zero total rotation are prescribed. See (2.9) in Sec. 2.1.3. The results are shown next.

# 5.1 Square cross–sections and radial forcing

In this subsection we assume that the cross-sections are squares, and optimize the stent width w and thickness h so that the resulting stent has minimal compliance, under the assumption that h = w. We apply an interior radial pressure force, uniform in magnitude along the entire stent, and study stent's response to this loading.

**Example 1.** We start by considering the simplest example of a stent consisting of a single zig-zag ring, as show in Fig. 5 left. The stent's length in this example is 0.0168022m, and the struts lie

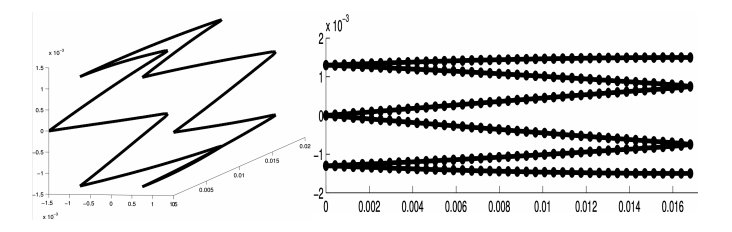


Figure 5: Zig-Zag stent. Left: The middle lines of the Zig-Zag stent. Right: Mesh points (struts discretization) with n = 40.

on a cylinder of radius 0.0015m. The total volume of this stent is equal to  $V_0 = 2.0185 \cdot 10^{-9} m^3$ . Each stent strut is split into n = 40 smaller struts, as shown in Fig. 5 right. The optimization algorithm is run with the initial configuration in which all the struts are of the same thickness. Fig. 6 left shows the expanded configuration of the reference stent in gray, and the expanded

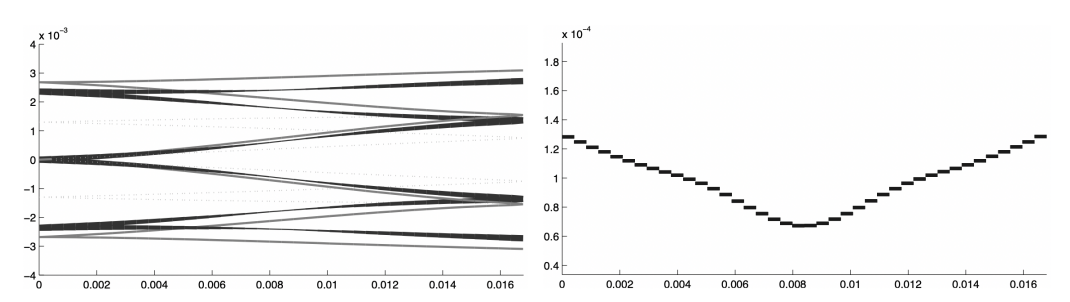


Figure 6: Left: Expanded configurations of a Zig-Zag stent with uniform strut thickness (gray), superimposed over the optimized stent with nonuniform strut thickness (black). Right: A graph showing strut thickness for the optimized stent, versus cylindrical axis of symmetry.

| Stent   | Init Compl.                    | Opt. Compl.                    | Min Thickness                 | Max Thickness                 | Fixed Vol.                      |
|---------|--------------------------------|--------------------------------|-------------------------------|-------------------------------|---------------------------------|
| Zig-Zag | $3.04 \cdot 10^{-5} \text{Nm}$ | $2.21 \cdot 10^{-5} \text{Nm}$ | $6.72 \cdot 10^{-5} \text{m}$ | $1.28 \cdot 10^{-4} \text{m}$ | $2.01 \cdot 10^{-9} \text{m}^3$ |

Table 1: Optimization of Zig-Zag stent, radial loading. The table shows initial compliance, optimal compliance for the stiffest stent, minimal and maximal stent strut thickness in the optimal stent, and the fixed volume used in the optimization algorithm.

optimal solution in black. One can observe that (1) the optimized stent indeed deforms less than the stent with uniform stent struts' thickness, and (2) the stent struts' thickness is larger at the joints of the stent. Detailed information about the strut's thickness is shown in Fig. 6 right and in Table 1. We can see that in the optimal configuration the minimal thickness of the struts is  $6.7219 \cdot 10^{-5}$ m, while the maximal is  $1.2856 \cdot 10^{-4}$ m. Compliance of the initial configuration of the stent with all struts of the same thickness is  $3.0411 \cdot 10^{-5}$ Nm, while the compliance for the optimized stent is  $2.21068 \cdot 10^{-5}$ Nm. This is a 45% increase in stent stiffness for the optimized stent.

Conclusion. This example shows that the stent's stiffness increases by the increase in the thickness of stent struts at the joints. This is to be expected since the radial pressure loading applied to the stent tends to increase the radius of the stents, which occurs due to bending of the struts in the plane tangential to the stent's cylinder. In Example 8 below, however, we will see that this fails to be true for the struts of very small thickness, see Fig. 14.

**Example 2.** Here we consider a more realistic stent of Palmaz-Schatz type, Palmaz6, which consist of six zig-zag rings in which all the struts are of the same length, see Fig. 7. The grey color in the left panel shows the expanded initial stent with stent struts of equal thickness, while the black color shows the optimized stents with the corresponding stent strut thickness leading to a stent with minimal compliance, expanded under the same loading density of f = 5000 N/m. Fig. 7 right shows strut thickness versus axis of symmetry of the stents' cylinder. The simulations were performed with n = 40 discretization points along each stent strut.

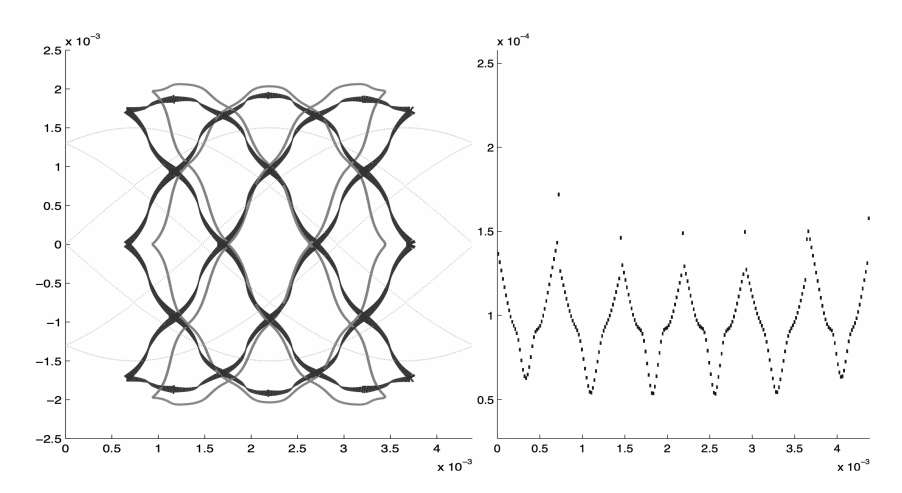


Figure 7: Palmaz6: Palmaz type stent under radial loading. The panel on the left shows the expanded initial configuration in grey and the optimal stent configuration in black. The panel on the right shows strut thickness versus axis of symmetry.

|         | 1         |                   |                                 | Max Thickness                     |                                    |
|---------|-----------|-------------------|---------------------------------|-----------------------------------|------------------------------------|
| Palmaz6 | 0.21771Nm | $0.15287 { m Nm}$ | $5.3401 \cdot 10^{-5} \text{m}$ | $1.7152 \cdot 10^{-4} \mathrm{m}$ | $7.7350 \cdot 10^{-10} \text{m}^3$ |

Table 2: Optimization of Palmaz like stent. The table shows initial compliance, optimal compliance for the stiffest stent, minimal and maximal stent strut thickness in the optimal stent, and the fixed volume used in the optimization algorithm.

Conclusions. We again see that the stiffest stents have struts with the thickness that is largest at the joints, and smallest at the mid-points of each strut. The precise data is shown in Table 2. Additionally, we also observe that the overall stiffness of the struts near the left and right edges of the stent is higher than everywhere else. This can be attributed to the compensation by the optimization algorithm of the so called dogboning effect, associated with the flaring-out of the stents' edges during uniform pressure loads during ballon angioplasty.

Example 3. Here we consider the geometry of a Cypher type stent. Cypher(TM) sirolimuseluting coronary stent is indicated for improving coronary luminal diameter in patients with symptomatic ischemic disease due to discrete *de novo* lesions of length  $\leq 30$ mm in native coronary arteries with reference vessel diameter between 2.2mm and 3.5mm. Cypher stent platform is made of 316L stainless steel material, with stent strut thickness of  $1.4 \cdot 10^{-1}$  mm [45]. The reference length of the stent considered in this study is 16.7mm and reference diameter 3mm. The stent consists of 8 zig-zag rings, connected via sinusoidal struts, see Fig. 8, forming seven circumferential cells.

We optimize the thickness of Cypher struts to maximize the stent's stiffness. We used n=10 discretization points for each strut. Fig. 8 shows the reference configuration (see Panel 1), the expanded initial configuration with struts of equal thickness (see Panel 2), the optimized Cypher stent with the corresponding struts' thickness (see Panel 3), and the graph of struts' thickness versus axis of symmetry (see Panel 4). Details of the optimization results are shown in Table 3.

Stent
 Init Compl.
 Opt. Compl.
 Min Thickness
 Max Thickness
 Fixed Vol.

 Cypher
 
$$0.8159 \text{Nm}$$
 $0.4101 \text{Nm}$ 
 $6.8486 \cdot 10^{-5} \text{m}$ 
 $2.6230 \cdot 10^{-4} \text{m}$ 
 $4.3535 \cdot 10^{-9} \text{m}^3$ 

Table 3: Optimization of Cypher stent, radial loading. The table shows initial compliance, optimal compliance for the stiffest stent, minimal and maximal stent strut thickness in the optimal stent, and the fixed volume used in the optimization algorithm.

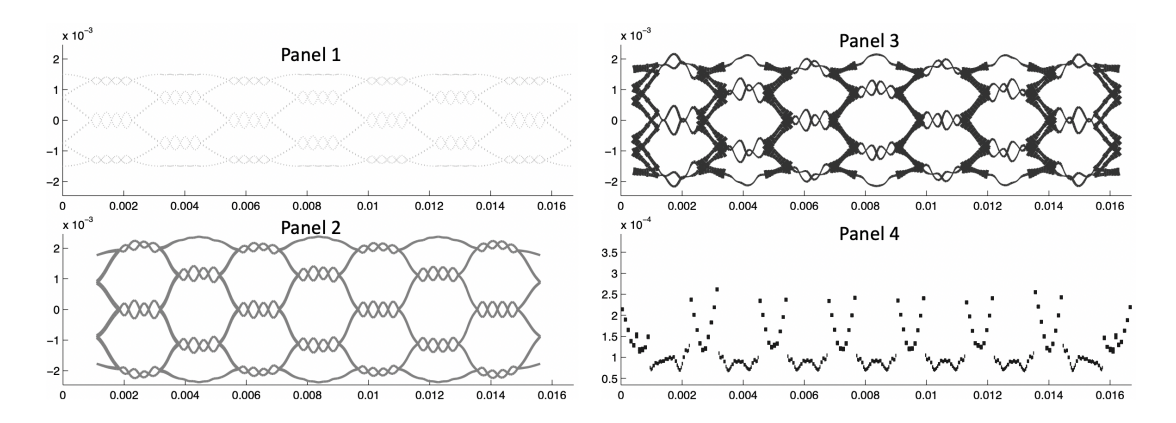


Figure 8: Cypher stent, radial loading. Panel 1: Reference configuration. Panel 2: Expanded Cypher stent with uniform strut thickness. Panel 3: Expanded Cypher stent with optimized strut thickness for maximal stiffness. Panel 4: Thickness versus axis of symmetry of the stent cylinder.

Conclusions. We see that the stiffest Cypher stent geometry is the geometry for which the zig-zag rings have thickness which is considerably higher than the thickness of the sinusoidal struts. See Fig. 8, Panel 4. The optimized expanded stent has a smaller maximal diameter (4.5mm) than the stent with uniform strut thickness (4.9mm). Additionally, the length of the expanded optimized stent is larger (15.9mm) and closer to the length of the original, reference stent (16.7mm) when compared to the length of the expanded stent with uniform strut thickness (14.5mm). The change in the length of the expanded stent is known as "foreshortening" and is an important piece of information when determining the size of the stent used to treat a lesion of a certain length. The smaller the foreshortening the better. We see that in terms of foreshortening, the optimized stent has preferred behavior over the non-optimized stent.

# 5.2 Square cross-sections and longitudinal forcing

In this section we consider stent optimization with respect to longitudinal forcing. The longitudinal loading is applied in a symmetric way stretching the stent in opposite directions with respect to its center line. The load is applied at every point of the stent.

**Example 4.** We start by considering the Palmaz type stent described in Example 2, above. Each stent strut is subdivided into n = 40 sub-segments, and a uniform longitudinal force density f = 5000N/m is applied in a symmetric way. The stent struts thickness is optimized to obtain the stiffest stents. Fig. 9 shows the results. Table 4 shows the initial and optimized values of

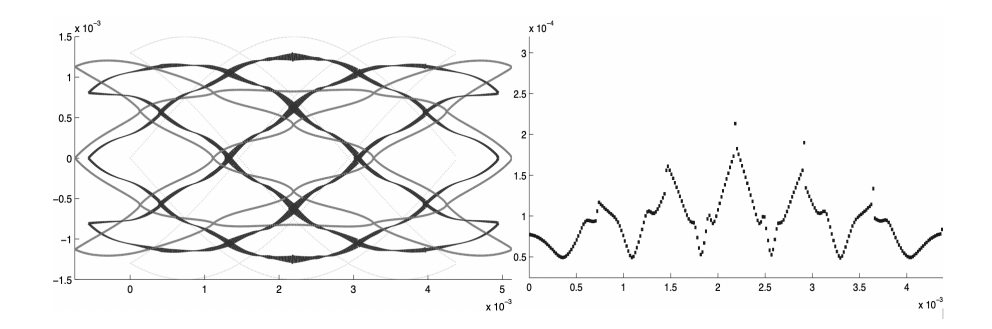


Figure 9: Palmaz6: Palmaz type stent, longitudinal loading. Left: expanded stent (initial configuration is in grey; optimal stent configuration is in black). Right: Strut thickness versus axis of symmetry.

the stent's compliance, and the minimal and maximal thickness of stent struts in the optimized stent. The fixed volume kept during the optimization procedure is the same as in Example 2.

|         |           |                        |                                 | Max Thickness                   |                                    |
|---------|-----------|------------------------|---------------------------------|---------------------------------|------------------------------------|
| Palmaz6 | 0.17181Nm | $0.094959 \mathrm{Nm}$ | $4.8647 \cdot 10^{-5} \text{m}$ | $2.1345 \cdot 10^{-4} \text{m}$ | $7.7350 \cdot 10^{-10} \text{m}^3$ |

Table 4: Optimization of Palmaz type stent. The table shows initial compliance, optimal compliance for the stiffest stent, minimal and maximal stent strut thickness in the optimal stent, and the fixed volume used in the optimization algorithm.

Conclusions. We see that under the symmetric longitudinal loading in opposite directions, the stiffest stent, namely the stent that resist the longitudinal stretching the most, is the stent with the thicker struts in the middle of the stent, and thinner struts at the edges of the stent, as shown in Fig. 9. This is exactly the opposite from the results shown in Example 2.

**Example 5.** Here we consider the same Cypher stent as discussed in Example 3, except that the stent is now subject to longitudinal loading. We used n = 10 discretization points for each strut, and the force density of f = 5000N/m was applied in opposite directions with respect to the central line of the stent. Fig. 10 shows the reference configuration (see Panel 1), the expanded initial configuration with struts of equal thickness (see Panel 2), the optimized Cypher stent with the corresponding struts' thickness (see Panel 3), and the graph of struts' thickness versus axis of symmetry (see Panel 4). Details of the optimization results are shown in Table 5.

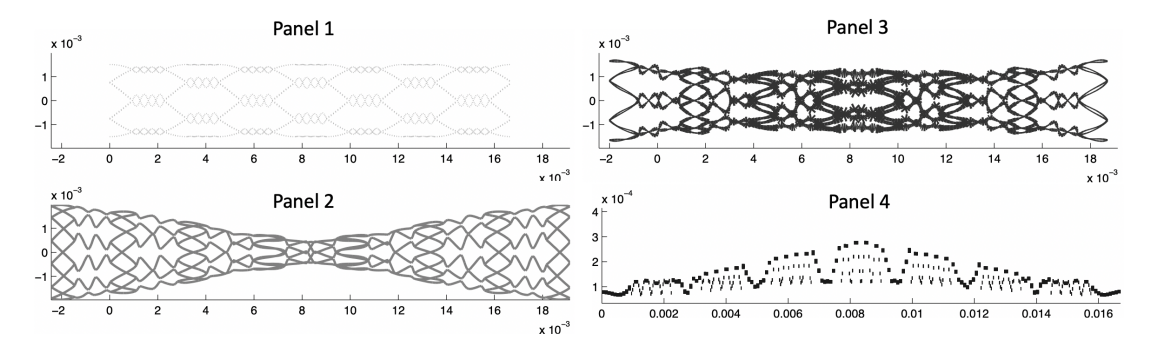


Figure 10: Cypher stent, longitudinal loading. Panel 1: Reference configuration. Panel 2: Expanded Cypher stent with uniform strut thickness. Panel 3: Expanded Cypher stent with optimized strut thickness for maximal stiffness. Panel 4: Thickness versus axis of symmetry of the stent cylinder.

Conclusions. We see that, as in Example 4, the stiffest stent is a stent with thick stent struts in the middle, and thinner struts at the end points. See Panel 4 in Fig. 10. Notice the

| Stent  | Init Compl. | Opt. Compl.      | Min Thickness                     | Max Thickness                     | Fixed Vol.                        |
|--------|-------------|------------------|-----------------------------------|-----------------------------------|-----------------------------------|
| Cypher | 1.7979Nm    | $0.9614 { m Nm}$ | $6.7753 \cdot 10^{-5} \mathrm{m}$ | $2.7635 \cdot 10^{-4} \mathrm{m}$ | $4.3535 \cdot 10^{-9} \text{m}^3$ |

Table 5: Optimization of Cypher stent, longitudinal loading. The table shows initial compliance, optimal compliance for the stiffest stent, minimal and maximal stent strut thickness in the optimal stent, and the fixed volume used in the optimization algorithm.

dramatically different behaviors of the optimized stent, shown in Panel 3 of Fig. 10, and the non-optimized stent, with uniform stent struts' thickness, shown in Panel 2 of Fig. 10. When compared with the results in Table 3 one can see that the maximal stiffness of the struts under the longitudinal loading is higher than the maximal stiffness of the struts in the optimized stent under radial loading.

# 5.3 Combined forcing and square cross–sections

In this section we apply different combinations of radial and longitudinal forcing on a single reference stent configuration corresponding to Palmaz type stent, and compare different optimal designs with respect to strut thickness for three different combinations of radial and longitudinal forcing. In each of the three cases we use n = 40 discretization points for each stent strut.

**Example 6.** We consider the following three cases of forcing applied to the Palmaz6 geometry:

$$\mathbf{f} = \alpha \mathbf{f}_r + \beta \mathbf{f}_l, \text{ where } \begin{cases} \alpha = 1, & \beta = 0.5; \text{ (Palmaz} 6_A), \\ \alpha = 1/\sqrt{2}, & \beta = 1/\sqrt{2}; \text{ (Palmaz} 6_B), \\ \alpha = 1, & \beta = 2; \text{ (Palmaz} 6_C), \end{cases}$$
(5.23)

where  $\mathbf{f_r}$  is radial forcing of density 5000N/m, and  $\mathbf{f_l}$  is longitudinal forcing of density 5000N/m, applied longitudinally in opposite directions with respect to the axial center point of the stent, stretching the stent in the left and right directions. The three different cases give rise to three substantially different stent configurations. See Figs. 11 and 12.

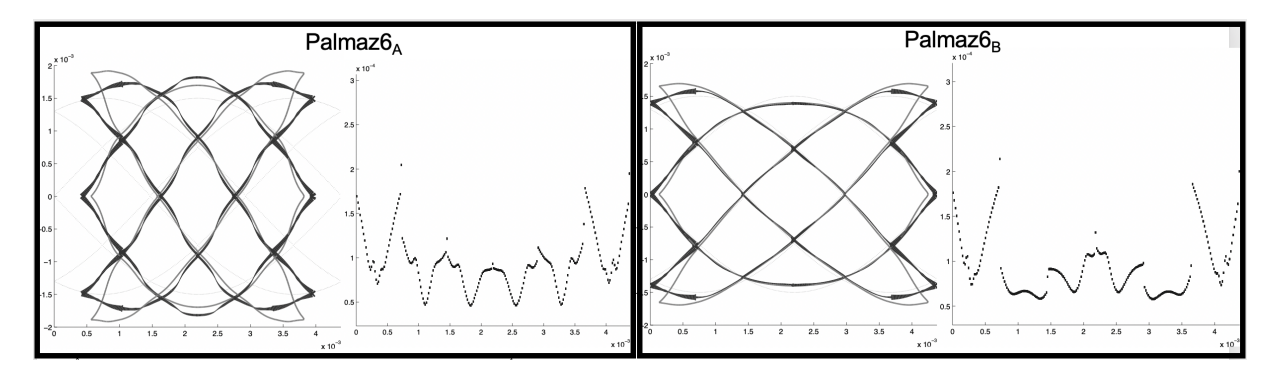


Figure 11: Left panel: Expanded Palmaz $6_A$  (left) and strut thickness versus symmetry axis (right). Right panel: Expanded Palmaz $6_B$  (left) and strut thickness versus symmetry axis (right).

Data associated with optimization of the three stents is shown in Table 6.

Conclusions. This example shows how different types of loading imply different optimal stent designs. Of particular interest is stent  $Palmaz6_C$ . The expanded structure, featuring flaring out of the end points with a rigid interior can be observed in stents designed to anchor bioartificial aortic valves, see Fig. 13. This shows that our optimization algorithm has the features necessary to produce optimal stent designs for different applications, including Transcatheter Aortic Valve Replacement (TAVR).

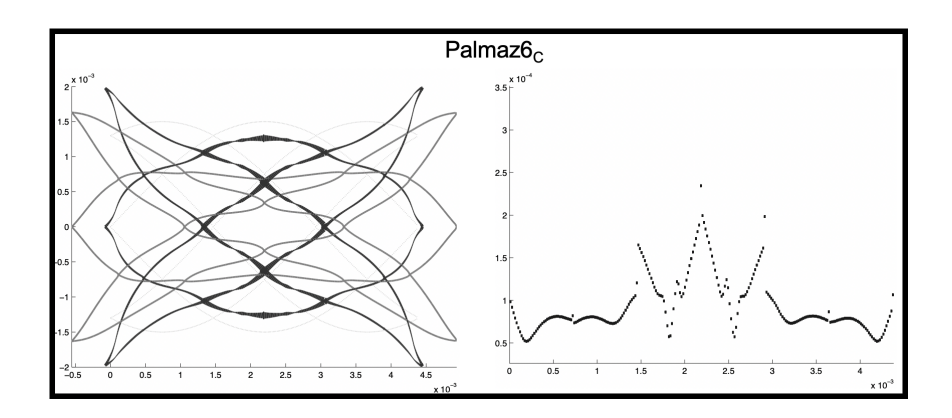


Figure 12: Left: Expanded Palmaz6<sub>C</sub> shown in black, superimposed over the expanded non-optimized Palmaz6 stent, under the loading with  $\alpha = 1$  and  $\beta = 2$  shown in (5.23). Right: Strut thickness for optimized stent Palmaz6<sub>C</sub> versus symmetry axis (right).

|                             |                        |                       |                                 | Max Thickness                   |                                    |
|-----------------------------|------------------------|-----------------------|---------------------------------|---------------------------------|------------------------------------|
|                             |                        |                       |                                 |                                 | $7.7350 \cdot 10^{-10} \text{m}^3$ |
| $\operatorname{Palmaz} 6_B$ | $0.021432 \mathrm{Nm}$ | $0.009966\mathrm{Nm}$ | $5.7611 \cdot 10^{-5} \text{m}$ | $2.1358 \cdot 10^{-4} \text{m}$ | $7.7350 \cdot 10^{-10} \text{m}^3$ |
| $Palmaz6_C$                 | $0.021164 \mathrm{Nm}$ | $0.0101\mathrm{Nm}$   | $6.057 \cdot 10^{-5} \text{m}$  | $2.3489 \cdot 10^{-4} \text{m}$ | $7.7350 \cdot 10^{-10} \text{m}^3$ |

Table 6: Optimization of Palmaz $6_A$ , Palmaz $6_B$ , and Palmaz $6_C$  stents. The table shows initial compliance, optimal compliance for the stiffest stent, minimal and maximal stent strut thickness in the optimal stent, and the fixed volume used in the optimization algorithm.

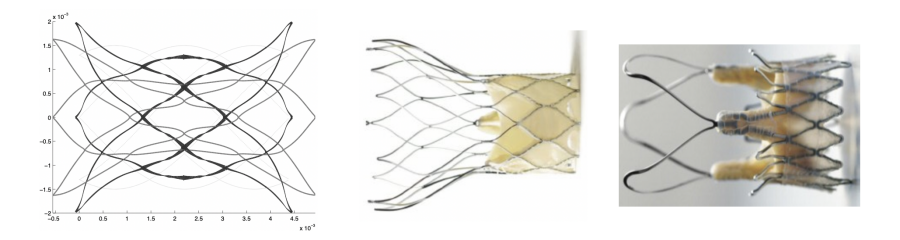


Figure 13: Left: Expanded Palmaz $6_C$ . Middle: Expanded aortic valve bioprosthesis Symetis Acurate  $TA^{TM}$ . Right: St. Jude Medical Portico TM Transcatheter aortic heart valve.

# 5.4 Radial forcing and rectangular cross–sections, optimization of struts' width over a series of tube thicknesses

Since balloon expandable stents are typically cut out of a metallic tube of a given thickness, in this section we optimize the stent struts' width, for a given tube thickness using methods explained in Sections 3.2 and 3.3. Thus, we allow that the cross-sections of stent struts be rectangles. This is different from the previous examples where the cross-sections of all struts were squares. In the end we perform optimization with respect to both the thickness of the tube and the width of stent struts and compare the optimal solution with the solutions obtained by fixing the tube thickness and optimizing only with respect to the strut width. Tables 7, 8, and 9 show the results for the three stents considered: the Zig-Zag stent, the Palmaz6 stent, and Cypher stent. The rows in red show the solutions for the optimization performed with respect to both the tube thickness and the strut width simultaneously. The rows in black show the solutions for the optimization performed only with respect to the strut width, for several tube thickness values.

**Example 7.** For the Zig-Zag stent we fix the total volume to be  $2.0185 \cdot 10^{-9} m^3$ , and run our optimization algorithm for four different tube thickness values between  $20 \mu m$  and  $100 \mu m$ .

Table 7 reports the results of those simulations, with an additional line, colored in red, showing optimal result for the optimization performed with respect to both thickness h of the tube and the width w of the stent struts. Fig. 14 shows the optimization results for the four different tube thickness values shown in Table 7 in black. Fig. 15 shows the optimal stent for the optimization with respect to both h and w, shown in red in Table 7. The corresponding 3D optimal stent, together with the initial configuration, are shown in Fig. 16. This optimal stent, which is

| Zig-Zag Tł                   |                   | Optimal Compliance               | Min Width                         | Max Width                         | Total Volume               |
|------------------------------|-------------------|----------------------------------|-----------------------------------|-----------------------------------|----------------------------|
| $0.2 \cdot 10^{-4} \text{m}$ | 1                 | $2.0972 \cdot 10^{-5} \text{Nm}$ | $3.8065 \cdot 10^{-4} \text{m}$   | $5.9645 \cdot 10^{-4} \text{m}$   | $2.0185 \cdot 10^{-9} m^3$ |
| $0.4 \cdot 10^{-4} \text{m}$ | 1                 | $9.2795 \cdot 10^{-6} \text{Nm}$ | $2.0131 \cdot 10^{-4} \text{m}$   | $3.1750 \cdot 10^{-4} \mathrm{m}$ | $2.0185 \cdot 10^{-9} m^3$ |
| $0.4738 \cdot 10^{\circ}$    | $^{-4}\mathrm{m}$ | $8.8700 \cdot 10^{-6} \text{Nm}$ | $1.3531 \cdot 10^{-4} \text{m}$   | $2.7907 \cdot 10^{-4} \mathrm{m}$ | $2.0185 \cdot 10^{-9} m^3$ |
| $0.5 \cdot 10^{-4} \text{m}$ | 1                 | $8.9492 \cdot 10^{-6} \text{Nm}$ | $1.3066 \cdot 10^{-4} \text{m}$   | $2.5520 \cdot 10^{-4} \text{m}$   | $2.0185 \cdot 10^{-9} m^3$ |
| $10^{-4} { m m}$             |                   | $1.9396 \cdot 10^{-5} \text{Nm}$ | $4.2475 \cdot 10^{-5} \mathrm{m}$ | $1.3810 \cdot 10^{-4} \text{m}$   | $2.0185 \cdot 10^{-9} m^3$ |

Table 7: Zig-Zag stent data for minimal compliance optimization. The numbers in black show the optimal results for the optimization with respect to the strut width w, for a given tube thickness h. The numbers in red show the optimal solution for the optimization with respect to both w and h.

the stiffest Zig-Zag stent made of a 316L stainless steel tube, occurs for the tube of thickness  $47.38\mu\text{m}$ . This optimal result corresponds to the red dot in Fig. 22 left, which shows the cost functional (compliance) vs. tube thickness for the Zig-Zag stent, optimized with respect to both h and w.

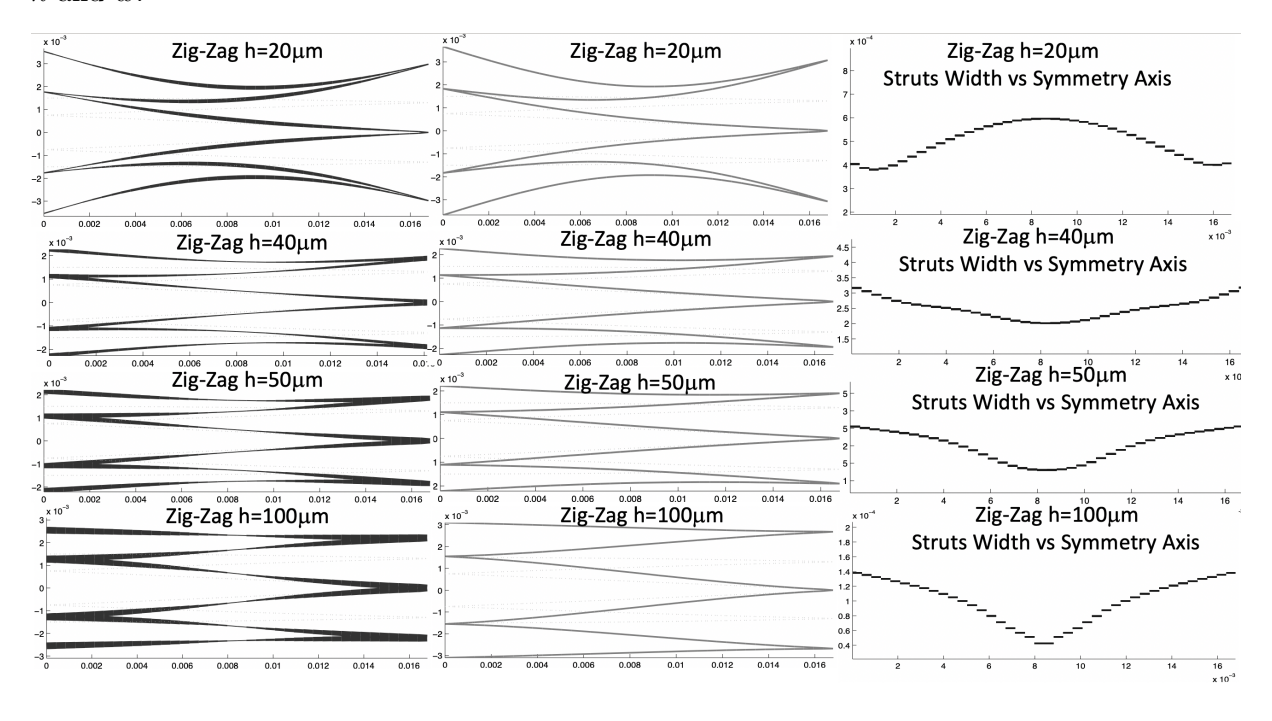


Figure 14: Zig-Zag stent. Left: Optimal stent; Middle: Starting configuration; Right: Strut width vs. axis of symmetry. The optimization is performed only with respect to the strut width w for four different values of h. See Table 7. Notice the stent for  $h = 20\mu m$ , which has struts whose width is largest in the middle, not at the junctions.

# Conclusions. Two interesting observations can be drawn:

1. From Fig. 14 we see that for very thin tubes, e.g.,  $h = 20\mu m$ , the stiffest stent has the struts that are widest in the middle than at the junctions. This is opposite from the stents that are cut out of a thicker tube with thickness  $h = 40\mu m$  and higher, shown in Fig. 14, for which the

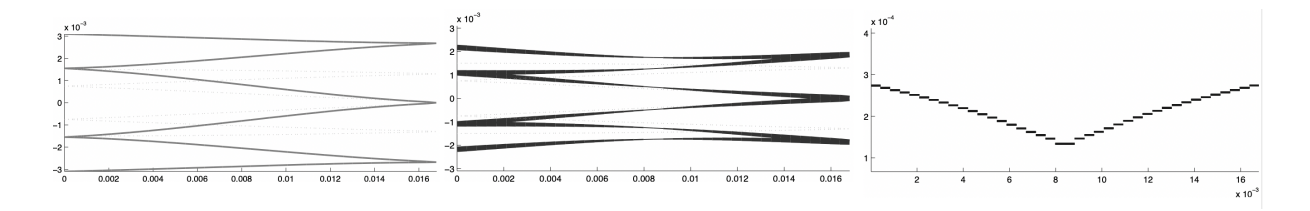


Figure 15: Zig-Zag stent optimized for both stent strut thickness and width, where the stent strut thickness is kept constant for the entire stent, motivated by the fact that balloon expandable stents are cut out of a metallic tube of constant thickness. Left: Initial configuration. Middle: Optimized stent. Right: Strut width vs. axis of symmetry. The minimal and maximal strut width and stent compliance are shown in red in Table 7.

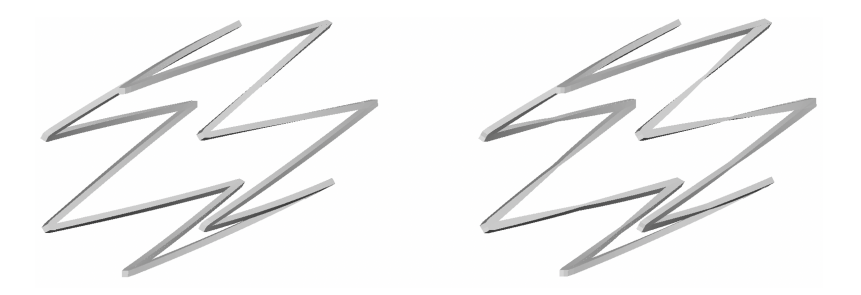


Figure 16: Zig-Zag stent: A comparison between the initial, non-optimal configuration with uniform thickness and struts' width (left), and optimized configuration (right). Both have the same material volume. The stent on the right has optimized tube thickness h and struts' width w giving the highest radial strength.

width of the struts is larger at the junction points than at the middle. Also, it is interesting to notice how the distribution of the widths of the struts changes as we increase the thickness of the tube, shown in the graphs on the right in Fig. 14.

2. When compared to the optimal stent from Example 1 for which h=w (square cross-sections), we see from Table 7 that optimal tube thickness in this example is smaller than the smallest thickness of the stent struts in Example 1:  $4.738 \cdot 10^{-5} \text{m} < 6.72 \cdot 10^{-5} \text{m}$ . However, this is compensated by the increase in the width of the stent struts in this example, when compared to Example 1. Namely, the width of the stent struts in this example is between  $1.3531 \cdot 10^{-4} \text{m}$  and  $2.7907 \cdot 10^{-4} \text{m}$ , while in Example 1 the width of the stent struts is between  $6.72 \cdot 10^{-5} \text{m}$  and  $1.28 \cdot 10^{-4} \text{m}$ . This is consistent with the constraint on the total volume of stent material. The resulting optimized compliance in this example is smaller than the optimized compliance in Example 1,  $8.8700 \cdot 10^{-6} \text{Nm}$  vs.  $2.21 \cdot 10^{-5} \text{Nm}$ . Therefore, we conclude that optimizing the Zig-Zag stent with respect to compliance by keeping the thickness of the metallic tube uniform along each stent, gives better solutions.

Example 8. Here we consider Palmaz6 stent. We optimize the struts' width for several thicknesses of the 316L stainless steel tubes to find the tube thickness and struts widths that correspond to the stiffest Palmaz6 stent. For all the stents in the optimization algorithm the total volume is kept at  $7.7350^{-10}m^3$ . Table 8 shows the data for seven different metallic tube thicknesses, with the row in red showing the optimal solution obtained, as in the previous example, by optimizing with respect to both the thickness h of the tube, and the width w of the struts. We see that the stiffest stent is obtained for the tube thickness of  $0.2854 \cdot 10^{-4}$ m, with the minimal and maximal width of stent struts between  $2.0138 \cdot 10^{-4}$ m and  $6.0470 \cdot 10^{-4}$ m. Fig. 17 shows the optimal stent in 2D, while Fig. 19 right shows its 3D image. This optimal result corresponds to the red dot in Fig. 22 middle, which shows the cost functional (compliance) vs. tube thickness for the Palmaz6 stent, optimized with respect to both h and w.

| Palmaz6 Thickness               | Optimal Compliance      | Min Width                         | Max Width                         | Total Volume      |
|---------------------------------|-------------------------|-----------------------------------|-----------------------------------|-------------------|
| $0.1 \cdot 10^{-4} \text{m}$    | $0.062135 \mathrm{Nm}$  | $4.4886 \cdot 10^{-4} \text{m}$   | $2.0369 \cdot 10^{-3} \text{m}$   | $7.7350^{-10}m^3$ |
| $0.2 \cdot 10^{-4} \text{m}$    | $0.029266\mathrm{Nm}$   | $3.0741 \cdot 10^{-4} \text{m}$   | $9.4024 \cdot 10^{-4} \text{m}$   | $7.7350^{-10}m^3$ |
| $0.2854 \cdot 10^{-4} \text{m}$ | $0.0244269 \mathrm{Nm}$ | $2.0138 \cdot 10^{-4} \text{m}$   | $6.0470 \cdot 10^{-4} \text{m}$   | $7.7350^{-10}m^3$ |
| $0.3 \cdot 10^{-4} \text{m}$    | $0.024632\mathrm{Nm}$   | $1.5760 \cdot 10^{-4} \mathrm{m}$ | $5.5991 \cdot 10^{-4} \text{m}$   | $7.7350^{-10}m^3$ |
| $0.4 \cdot 10^{-4} \text{m}$    | $0.029452 \mathrm{Nm}$  | $8.5846 \cdot 10^{-5} \text{m}$   | $4.0752 \cdot 10^{-4} \mathrm{m}$ | $7.7350^{-10}m^3$ |
| $0.6 \cdot 10^{-4} \text{m}$    | $0.052715 { m Nm}$      | $3.5213 \cdot 10^{-5} \text{m}$   | $2.6637 \cdot 10^{-4} \text{m}$   | $7.7350^{-10}m^3$ |
| $10^{-4} { m m}$                | $0.13360\mathrm{Nm}$    | $1.3587 \cdot 10^{-5} \text{m}$   | $1.6096 \cdot 10^{-4} \mathrm{m}$ | $7.7350^{-10}m^3$ |

Table 8: Palmaz6 stent data for minimal compliance optimization with respect to stent strut thickness and stent strut width, where the thickness is kept constant along each stent.

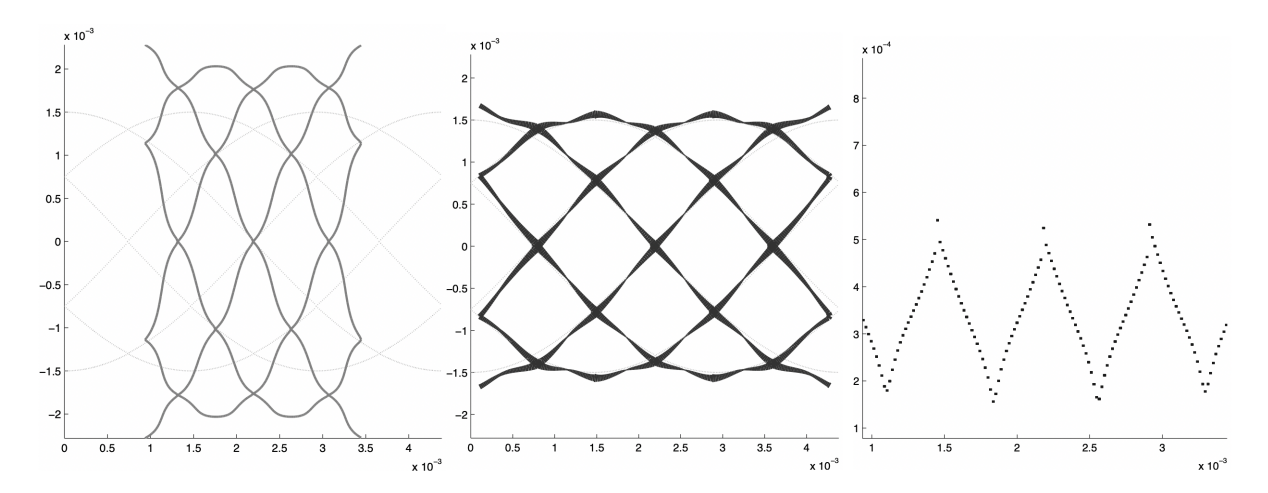


Figure 17: Palmaz6 stent optimized for both stent strut thickness and width, where the stent strut thickness is kept constant for the entire stent, motivated by the fact that balloon expandable stents are cut out of a metallic tube of constant thickness. Left: initial configuration. Middle: Optimized stent. Right: Strut width vs. axis of symmetry.

Similarly as in the previous example, in the case of a very thin tube, namely for  $h = 10\mu\text{m}$ , see Fig. 18, the optimal stent has struts that are wider in the middle than at the joints. This is opposite to all the other stents for which  $h \geq 20\mu\text{m}$ . Fig. 18 shows a comparison between the thin stent for which  $h = 10\mu\text{m}$  and the optimal stent, shown in Fig. 17, fully expanded. Notice how the deformation under uniform pressure loading is different for the two stents: significant radial deformation can be seen for the stent with  $h = 10\mu\text{m}$ .

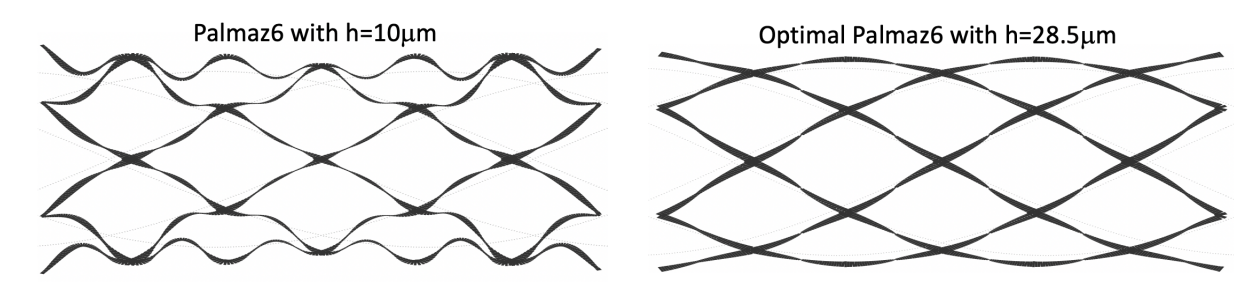


Figure 18: Comparison between the fully expanded Palmaz6 stent cut out of a very thin tube  $(h = 10\mu m)$  shown on the left, and the optimal stent from Fig. 17 shown on the right. Notice that for the  $h = 10\mu m$  stent, the struts are thicker in the middle, they become thinner near the joints, and then thick again at the joints. Additionally, significant radial deformation of the stent with  $h = 10\mu m$  can be observed, which is not visible in the optimal stent shown on the right.



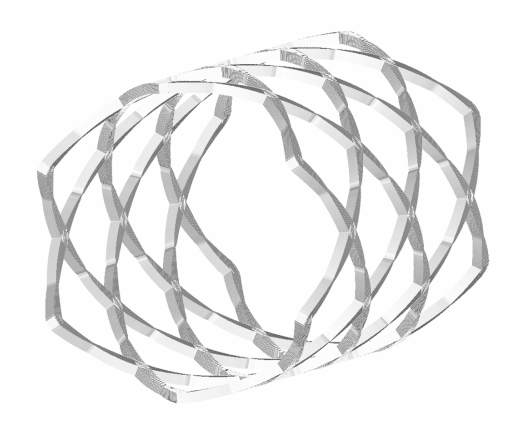


Figure 19: Palmaz6 stents: A comparison between the initial, non-optimal configuration with uniform thickness and width of stent struts, shown on the left, and the optimized configuration corresponding to the red line in Table 8, shown on the right. Both have the same material volume. The stent on the right has optimized tube thickness h and strut width w giving the highest radial strength.

#### **Conclusions.** Two interesting observations can be drawn:

- 1. From Fig. 18 left we see that for very thin tubes, e.g.,  $h = 10\mu m$ , the stiffest stent has the struts that are widest in the middle, they become thinner near the joints, and then thick again at the joints. As a result the deformation under uniform pressure loading is significantly different from the deformation of the optimal stent, shown in Fig. 18 right. Notice how the centers of the struts have smaller radial displacement than the joints of the stent. This is very different from the deformed stent shown on the right.
- 2. When compared to the optimal Palmaz6 stent from Example 2, we draw similar conclusions as for the Zig-Zag stent above. The optimal tube thickness in this example is smaller than the smallest thickness of stent struts in Example 2, however, this is compensated by the increase in the width of stent struts in this example, when compared to Example 2. The resulting optimized compliance in this example is significantly smaller than the optimized compliance in Example 2, 0.0244269Nm vs. 0.94959Nm, which is a reduction of 38 times in compliance achieved by the stent in Fig. 17. We conclude that optimizing the Palmaz6 stent with respect to compliance by keeping the width of the metallic tube uniform along each stent, provides significantly better results, as was the case with the Zig-Zag stents in the previous example.

**Example 9.** Here we consider Cypher stent. We optimize the struts' width for several thicknesses of the 316L stainless steel tubes to find the tube thickness and struts widths that correspond to the stiffest Cypher stent. For all the stents in the optimization algorithm the total volume is kept at  $4.3535 \cdot 10^{-9} m^3$ . The initial thickness was taken to be  $1.4 \cdot 10^{-4} m$ . Table 9

| Cypher Thickness                  | Optimal Compliance    | Min Width                         | Max Width                         | Total Volume               |
|-----------------------------------|-----------------------|-----------------------------------|-----------------------------------|----------------------------|
| $0.4 \cdot 10^{-4} \text{m}$      | 0.69161Nm             | $1.9212 \cdot 10^{-5} \mathrm{m}$ | $8.3330 \cdot 10^{-4} \text{m}$   | $4.3535 \cdot 10^{-9} m^3$ |
| $0.6 \cdot 10^{-4} \text{m}$      | $0.37138\mathrm{Nm}$  | $1.4607 \cdot 10^{-5} \mathrm{m}$ | $5.1185 \cdot 10^{-4} \text{m}$   | $4.3535 \cdot 10^{-9} m^3$ |
| $0.8 \cdot 10^{-4} \text{m}$      | $0.27389 \mathrm{Nm}$ | $1.0635 \cdot 10^{-4} \mathrm{m}$ | $4.3553 \cdot 10^{-4} \text{m}$   | $4.3535 \cdot 10^{-9} m^3$ |
| $1.0 \cdot 10^{-4} \text{m}$      | 0.24717 Nm            | $6.6646 \cdot 10^{-5} \text{m}$   | $3.8404 \cdot 10^{-4} \text{m}$   | $4.3535 \cdot 10^{-9} m^3$ |
| $1.0282 \cdot 10^{-4} \mathrm{m}$ | $0.24628\mathrm{Nm}$  | $5.7496 \cdot 10^{-5} \text{m}$   | $3.6928 \cdot 10 - 4 \text{m}$    | $4.3535 \cdot 10^{-9} m^3$ |
| $1.2 \cdot 10^{-4} \text{m}$      | $0.25031\mathrm{Nm}$  | $4.8512 \cdot 10^{-5} \mathrm{m}$ | $3.2200 \cdot 10^{-4} \mathrm{m}$ | $4.3535 \cdot 10^{-9} m^3$ |
| $1.4 \cdot 10^{-4} \text{m}$      | $0.27048 \mathrm{Nm}$ | $2.8829 \cdot 10^{-5} \mathrm{m}$ | $2.8067 \cdot 10^{-4} \mathrm{m}$ | $4.3535 \cdot 10^{-9} m^3$ |

Table 9: Cypher stent data for minimal compliance optimization with respect to stent strut thickness and stent strut width, where the thickness is kept constant along each stent.

shows the optimization results, with the line in red showing the optimal solution obtained by

changing both h and w, where h is kept fixed over the entire stent. The optimal stent data is shown in Fig. 20, and a 3D image of the optimal stent is shown in Fig. 21. Fig. 21 also shows a comparison with the initial, non-optimal configuration.

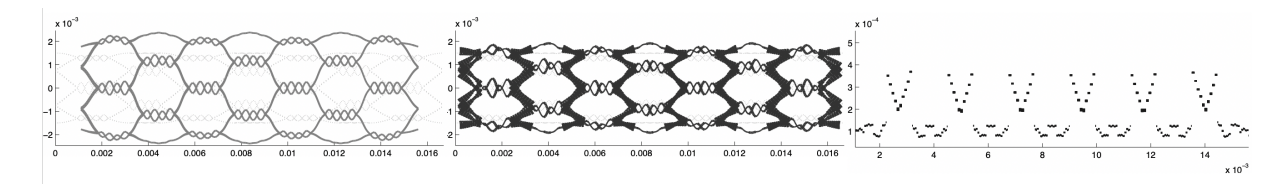


Figure 20: Cypher stent optimized for both stent strut thickness and width, where the stent strut thickness is kept constant for the entire stent, motivated by the fact that balloon expandable stents are cut out of a metallic tube of constant thickness. Left: Initial configuration. Middle: Optimized stent. Right: Strut width vs. axis of symmetry.



Figure 21: Cypher: A comparison between the initial, non-optimal configuration with uniform thickness and width of stent struts (left), and optimized stent (right). Both have the same material volume. The stent on the right is optimized with respect to the tube thickness h and stent struts' width w. In this stent, the thickness of the sinusoidal connecting struts is roughly 1/3 of the thickness of the zig-zag rings.

Conclusions. By comparing the results from Example 3 and this example, we conclude that optimizing Cypher stent with respect to compliance by keeping the width of the metallic tube uniform along each stent, provides significantly better results, as was the case with the previous two examples. Namely, Table 9 shows that optimal compliance of the Cypher stent in this example is 0.24628Nm, which is 50% smaller than optimal compliance of the Cypher stent in Example 3. As in Example 3, the zig-zag rings in Cypher stent are responsible for bearing most of the load in uniform pressure loading, with the ratio between the average thickness of the thin sinusoidal struts and the average thickness of the zig-zag struts in the optimal configuration being roughly equal to 1:3, see Table 9. This is similar to what is used in the production of certain Cyphers stents, see [29].

We conclude this section by the graphs shown in Fig. 22, which depict compliance vs. tube thickness for the three stents. We observe that the cost function (compliance) appears to be a convex function of the tube thickness, and that the minimum, which is denoted by the red dot in each of the three graphs, is significantly lower for the Palmaz6 stent than for the other two stents, showing a well-accepted opinion that Palmaz-like stents are the stiffest stents on the US stent market.

# 6 Comparison with a Genetic Algorithm

We compared the results and efficiency of our optimization algorithm with the genetic algorithm implemented in Matlab 2010a, run on the same personal computer as the optimization algorithm used above, with 2.4 GHz Quad-Core Intel Core i5 and 16 GB 2133 MHz LPDDR3 memory. The comparison was performed for the Zig-Zag stent problem presented in Example 1.

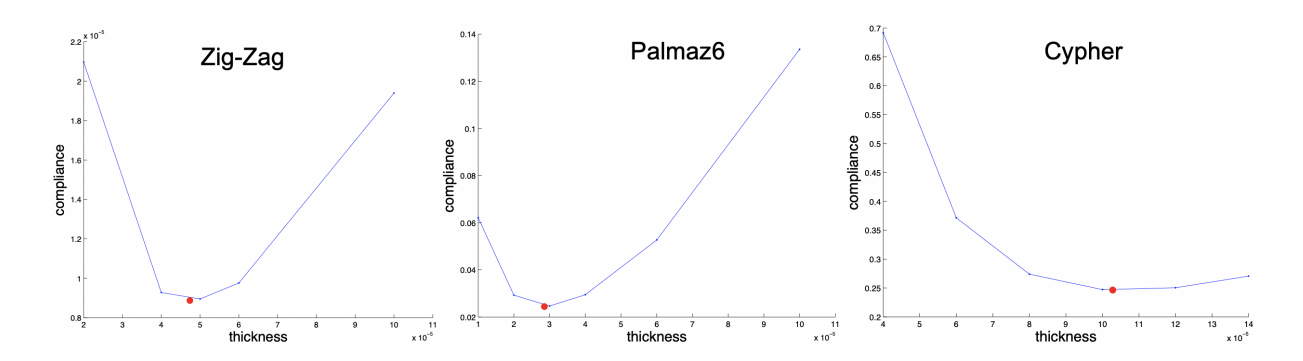


Figure 22: Cost functional (compliance) versus tube thickness for Examples 7, 8, and 9, with the optimum denoted by the red dot. The plots indicate that in all three examples compliance is a convex function of tube thickness. By comparing the stiffness values for the optimal configurations, we see that of the three stents, the stiffest one is Palmaz6.

For the Zig-Zag stent, each strut was divided into six subintervals. Each subinterval carried information about the thickness of that subinterval. This defines six degrees of freedom in the optimization algorithm for each strut. Since the entire Zig-Zag stent consists of twelve struts, the optimization problem we considered had 72 degrees of freedom. To lower the computational cost of the entire stent optimization procedure, we used the fact the the pressure loading is symmetric, and identified one strut with all the remaining eleven struts forming the Zig-Zag stent shown in Fig. 5. More precisely, the substruts (subintervals) with the same  $\{x_1\}_{start}$  and  $\{x_1\}_{end}$  (axial) coordinates were identified among different struts. This way the number of degrees of freedom for the entire stent was kept at only six (corresponding to one strut), providing a symmetric solution. In fact, we noticed that the genetic algorithm was having difficulties keeping the solution symmetric without the approach described above. This is a well-known downside of genetic algorithms. However, it is important to notice that this is different from the algorithm studied in the present paper. We never needed to impose a symmetric solution in any of the examples presented above. The symmetries in our algorithm are embedded in the formulation of the optimization problem.

We ran the genetic algorithm with no initial data prescribed, using 200 generations and a population size of 100. Optimization was performed by changing the width of the stent struts with the tube thickness of  $h = 10^{-4} \text{m} = 100 \mu \text{m}$ . We obtained an optimized stent with the minimal compliance equal to  $2.13417 \cdot 10^{-5} \text{Nm}$ , and stent strut thickness for each of the six intervals along each strut given by:

Stent
 
$$w_1$$
 ( $\mu$ m)
  $w_2$  ( $\mu$ m)
  $w_3$  ( $\mu$ m)
  $w_4$  ( $\mu$ m)
  $w_5$  ( $\mu$ m)
  $w_6$  ( $\mu$ m)

 Zig-Zag
 142.9711
 101.2637
 67.1848
 61.9685
 100.3653
 126.8807

The graphs shown in Fig. 23 show optimal strut width v.s. strut length obtained using the genetic algorithm (left) and our algorithm (right).

One can notice three things:

- 1. The symmetry of the strut width along each strut in the genetic algorithm is not kept as well as it is in our algorithm (compare  $w_1$  with  $w_6$ ,  $w_2$  with  $w_5$ , and  $w_3$  with  $w_4$ ).
- 2. The minimal compliance obtained using the genetic algorithm, which was equal to  $2.13417 \cdot 10^{-5}$ Nm, is higher than the minimal compliance obtained using our algorithm, which was  $2.120925 \cdot 10^{-5}$ Nm, which indicates that the results of our algorithm are closer to the true minimum.
- 3. The time it took the genetic algorithm to generate the optimal solution was 280 seconds, which is 60 times longer than 4.5 seconds it took our optimization algorithm to run on the

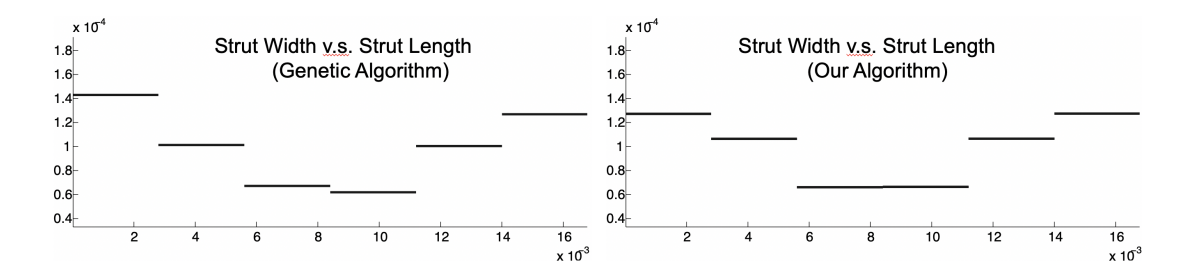


Figure 23: Comparison between the genetic algorithm and our algorithm: strut width v.s. strut length.

same machine. In fact, the 4.5 seconds is the time it took our algorithm to optimize the stent *without* any assumptions on the symmetry of the problem, thereby computing with 72 degrees of freedom (72 = 2 (ends of each subinterval) \*6 (subintervals) \*6 (struts)), instead of the 6 degrees of freedom used in the genetic algorithm to enforce symmetry.

In conclusion, we argue that for the class of optimization problems considered here, where the stent is modeled using the *one-dimensional stent net model* [39], the algorithm proposed in this manuscript outperforms the genetic algorithm in three key features: (1) computational time, (2) accuracy, and (3) symmetry.

For longer stents, and more degrees of freedom, the genetic algorithm may not be an option due to the prohibitively large computational time and asymmetries that contaminate the solution landscape.

# 7 Strain information for optimized configurations

Finally, we present strain information for the optimized configurations shown in Figures 15, 19, and 21. The strain magnitude in this 1D model is proportional to  $\|\partial_s \omega\|$ , see [26]. A simple argument which relates strain to  $\partial_s \omega$  can be explained as follows. Following the derivation of the Antman-Cosserat 1D curved rod model from 3D elasticity presented in Antman [4] and Scardia [36], one can see that the following quantity:  $[\partial_s \mathbf{R}] \mathbf{R}^T$ , plays the main role in the calculation of strain, where R is a rotation matrix that describes the behavior of the cross-section of the rod. The quantity  $[\partial_s \mathbf{R}] \mathbf{R}^T$  measures flexure and torsion of the middle curve of the curved rod. Since R is a rotation matrix function, there exists a vector function  $\omega$  such that  $\mathbf{R} = e^{\mathbf{A}\omega}$ , and  $\mathbf{A}_{\omega}$  denotes the skew-symmetric matrix with axial vector  $\boldsymbol{\omega}$  ( $\mathbf{A}_{\omega}x = \boldsymbol{\omega} \times x$ ). A simple calculation then shows that  $[\partial_s \mathbf{R}] \mathbf{R}^T = \mathbf{A}_{\partial_s \boldsymbol{\omega}}$ , where this  $\boldsymbol{\omega}$  is exactly the same as the  $\boldsymbol{\omega}$  we use in the stent model. The typical remaining strains are zero in the model (2.12) we use, as was rigorously justified in [36], since we have inextensibility and unshearability assumed in the Therefore, to capture the strain magnitude in this reduced 1D model, it is sufficient The pictures presented in this section show  $\|\partial_s \boldsymbol{\omega}\|$  for the non-optimized and optimized configurations of the stents shown in Figures 15, 19, and 21. The strains are presented on deformed configurations.

We start with the strain associated with the Zig-Zag stent shown in Figure 15. We see that for the Zig-Zag stent, the optimization procedure minimizing compliance gives rise to a stent for which the maximal strain is comparable to the non-optimized configuration, however, the distribution of strain is "the opposite" to the non-optimized stent. While the non-optimized stent has maximal strain concentrated at the joints of the stent, the optimized stent's maximal strain occurs in the middle of the stent struts. This is because the centers of the struts in the optimized stent are thinner then in the non-optimized stent.

In Figure 25 we show strain distribution for the Palmaz6 stent. One can see that the expanded optimized stent has maximal strain that is 24% smaller than the non-optimized stent.

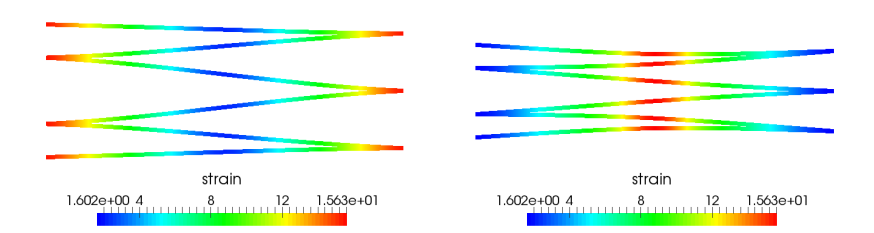


Figure 24: Zig-zag stent from Figure 15. Left: Strain for the non-optimized stent, with maximum strain 15.4m<sup>-1</sup>. Right: Strain for the optimized stent, with maximum strain 15.6m<sup>-1</sup>. While the max strain for the two configurations has not changed in a significant way, the concentration of high strain has moved from the joints in the non-optimized stent, to the middle of the struts in the optimized configuration. This is because centers of the struts in the optimized stent are thinner then in the non-optimized stent.

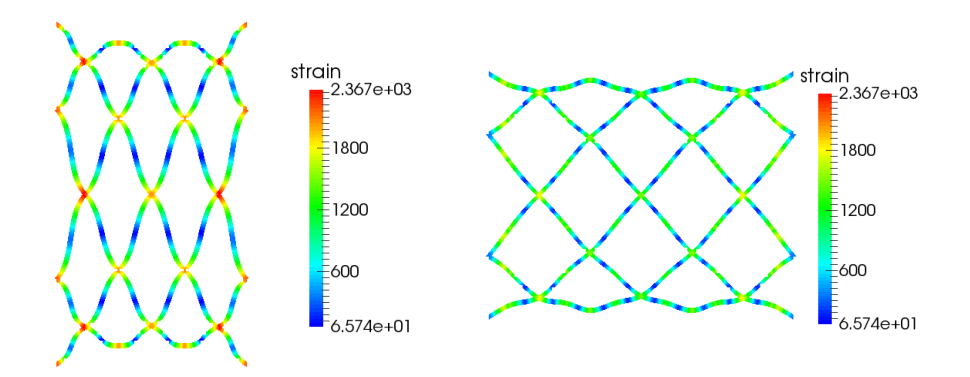


Figure 25: Palmaz stent from Figure 19. Left: Strain for the non-optimized stent, with maximum strain  $2367m^{-1}$ . Right: Strain for the optimized stent, with maximum strain  $1787m^{-1}$ , which is a reduction in maximal strain of 24%. While the maximal strain is located at the joints for both configurations, the strain distribution along the stent struts is different for the nonoptimal and optimal stent configurations.

We also observe that the maximal strain is concentrated at the joints of the stent for both configurations.

Finally, we present the strain distribution for Cypher stent. We observe that the optimized

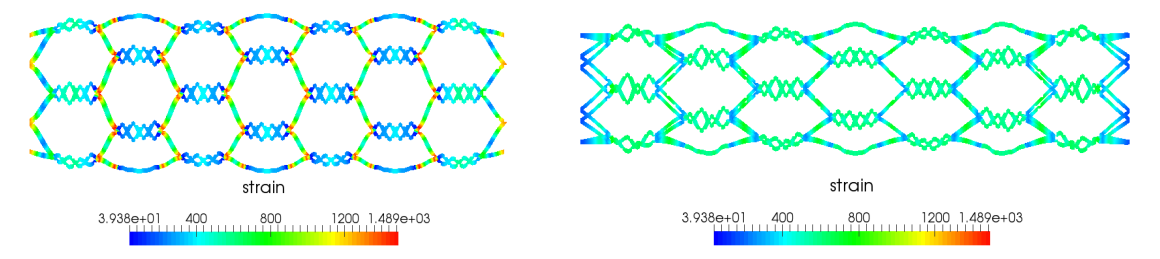


Figure 26: Cypher stent from Figure 21. Left: Strain for the non-optimized stent, with maximum strain 1489m<sup>-1</sup>. Right: Strain for the optimized stent, with maximum strain 754m<sup>-1</sup>, which is a reduction in maximal strain of 49%. In contrast with the non-optimized configuration where the maximum strain is located at the stents joints, the maximal strain in the optimized stent is distributed along the struts.

Cypher stent has maximal strain that is 49% smaller than the maximal strain of the non-optimized configuration. Additionally, we see that the maximal strain concentration has shifted from the joints of the stent to the centers of the stent struts, making this stent a desirable choice for the lesions in which stent stiffness and low strain at stent joints is preferred.

# 8 Conclusions

We conclude this manuscript with a summary of the main results of the paper (see subsection 8.1), and a comparison of the proposed optimization approach based on the 1D reduced model discussed here, with a full 3D approach recently published by Russ et al. in [35] (see subsection 8.2.

#### 8.1 Summary

In Section 2 we introduced the differential and integral (weak) formulations of the 1D stent model. Based on this 1D stent model, we formulated a constrained optimization problem in Section 3. The constrained optimization problem is based on minimizing compliance for the three stents considered in this study: the Zig-Zag stent, the Palmaz6 stent, and a Cypher-like stent. We presented three sets of minimization procedures: the first one assumes that the cross-sections of the stent struts are squares, and optimizes the squares' sides h (see Section 3.1), the second one assumes that the cross-sections of the stent struts are rectangles, with constant thickness h, and optimizes the widths  $w_i$  of each stent strut (see Section 3.2), and the third assumes that the cross-sections of the stent struts are rectangles, and optimizes with respect to both the stent thickness h and the width  $w_i$  of each stent strut (see Section 3.3). In the first case a proof of the existence of a unique minimizer was obtained in Section 3.4. For all three cases a numerical optimization algorithm was developed, with the main steps of the algorithm shown in (3.20). A Finite Element Method-based numerical method was developed and described in Section 4, where a series of numerical results, providing insightful information about optimal stent design, were presented. The following is a snapshot of those results:

1. Minimal compliance under radial force for the stents manufactured from stainless steel tubes of thickness  $40\mu m$  and higher, is achieved by increasing the width of stent struts near the struts' joints. For the thin struts whose thickness is between  $10\mu m$  and  $20\mu m$ , which appears to be a popular choice currently, the stiffest stent has the struts that are wider in the middle than at the joints. For very thin struts, whose thickness is  $10\mu m$  or

smaller, the stiffest stent has the struts that are widest in the middle, then become thinner as we approach the junction, and are again thick at the joints.

- 2. Minimal compliance under a symmetric *longitudinal force* (stretching) is achieved with the stents that have thicker struts near the center of the stent, and thinner struts at the edges of the stent.
- 3. For Palmaz-Schatz-like stents, which are stents with a uniform geometry, the stent compliance is minimal for the stents with thicker struts near the left and right edges of the stents. This is directly related to the dogboning effect associated with the flaring-out of the stents edges under uniform pressure loading during balloon angioplasty.
- 4. The stiffest Cypher-like stent geometry is the geometry for which the zig-zag rings have thickness which is considerably higher than the thickness of the sinusoidal struts. This is in line with the most recent designs of Cypher-like stents that are currently available on the US market, see [29]. Our analysis suggests that the optimal thickness ratio between the zig-zag struts and the sinusoidal struts is 3:1.
- 5. For both Palmaz6 and Cypher stents, the optimal configurations presented in this work have maximal strain that is significantly lower than the strain of the non-optimized configuration. See Section 7. Lower strain could be associated with lower fatigue in those stents (not analysed in this work).
- 6. Based on these findings, the optimized Cypher-like stent presented in Figure 21, could, in fact, be a realistic choice for stent implantation in lesions where radial strength, flexibility to bending, and low junction fatigue are preferred.

#### 8.2 Comparison with 3D surrogate-based optimization approaches

Finally, we compare our approach with 3D surrogate-based approaches, such as those used in [35]. The work presented in [35] discusses optimization of a stent used to anchor a pediatric balloon-expandable prosthetic heart valve. The optimization is performed with respect to three parameters: uniform stent strut thickness, uniform stent strut width, and the number of circumferential patterns. The goal in [35] is to obtain a stent that is stiff enough to counteract the retraction of a polymeric glue that holds a prosthetic heart valve, under a constraint on the stent diameter to be as uniform as possible, and as close to the diameter of the remaining conduit as possible. Additionally, a criterion for ductile failure was incorporated in the computational model. Optimization was performed on a 3D stent model, which was approximated by a high quality hexahedral mesh. The optimization algorithm was a surrogate-based multi-objective optimization procedure.

Because of the high **computational costs** typically associated with 3D approaches the run time is typically hours for each model evaluation without a high quality preconditioner, see [35]. This can be compared to 1-2 seconds that it takes for the reduced 1D model evaluation using a serial code on a laptop with a 2.4 GHz Quad-Core Intel Core i5 and 16 GB 2133 MHz LPDDR3 memory. The *entire optimization algorithm* presented in this manuscript takes 3-5 minutes on this laptop.

The significantly shorter simulation time of the 1D model allows the use of a large **number** of optimization parameters. In the present paper, since the strut thickness and width are *not uniform*, the number of optimization parameters is, in fact, 2880. It would be computationally prohibitive to take into account 3000 parameters in the 3D approaches using surrogate-based optimization.

Another significant difference between the two approaches is the way how the optimization procedure accounts for the dependence of the cost function on the optimization parameters. While a surrogate-based model alla Russ et al. [35] contains information about the model

parameters implicitely, the model presented in this manuscript provides an explicit dependence of the cost function on the parameters in the problem. This reduces the computational costs significantly. At most 100 iterations are needed to complete the optimization procedure based on a gradient descent method, which translates into the total computational time of only a few minutes per stent optimization with high accuracy. Furthermore, rigorous mathematical analysis presented in this manuscript guarantees that the problem is **well-posed**, which implies that the problem we are solving actually has a minimum, thereby justifying the development of a computational algorithm to solve it.

Because of the simplicity of the 1D model, which can be viewed as a rigorously justified "surrogat" model for the 3D problem, we are also not restricted by the size of the optimization step in the gradient descent-based algorithm to find the minimum. Due to the rigorous derivation of the 1D "surrogat" model in [20, 39], our approach contains the information that allows us to deal with even local oscillatory behavior of the cost function near a minimum.

In summary, the advantages of the proposed algorithm are its computational efficiency, a capability to handle a large number of optimization parameters, high accuracy, and confidence based on mathematical rigor implying that the minimum we are looking for actually exists. Drawbacks include the lack of detailed 3D information within each stent strut that is provided by full 3D simulations.

The ultimate goal of this research would be to design a *hybrid* algorithm based on both approached. First, one would identify the extrema of the cost function using the efficient 1D-based model that captures explicitly the parameter landscape and the dependence of the cost function on the parameters, presented in this manuscript. Once a minimum is found, 3D approaches, such as those presented in Russ et al. [35] would be used to explore a neighborhood around the minimum in order to capture the full 3D information of the optimizer that may not be available from the 1D reduced model approach.

# Acknowledgments

The authors would like to thank Marko Vrdoljak for the helpful discussions and comments. Partial funding for this work was provided by the National Science Foundation, under grants DMS-1853340 (Čanić and Tambača), and DMS-2011319 (Čanić). Partial support was also provided by the Croatian Science Foundation under grant IP-2018-01-2735 (Ljulj and Tambača), and under grant IP-2019-04-6268 (Grubišić). The authors would also like to acknowledge the support by a Cro-USA grant 1/2020 (Grubišić, Ljulj and Tambača).

# References

- [1] G. Allaire, Conception optimale de structures. Springer-Verlag, Berlin, 2007.
- [2] G. Allaire. Optimal Design of Structures, MAP 562, Chapter 4 Department of Applied Mathematics, Ecole Polytechnique. January 14, 2015. http://www.cmap.polytechnique.fr/~allaire/course\_map562.html
- [3] C. D'Angelo, P. Zunino, A. Porpora, S. Morlacchi, F. Migliavacca, Model reduction strategies enable computational analysis of controlled drug release from cardiovascular stents. *SIAM Journal on Applied Mathematics* 71(6) 2312–2333, 2011.
- [4] S. S. Antman, Nonlinear Problems of Elasticity, Springer-Verlag, 1995.
- [5] F. Auricchio, M. Conti, M. Ferraro, S. Morganti, A. Reali, R. L. Taylor. Innovative and efficient stent flexibility simulations based on isogeometric analysis. *Comput. Methods Appl. Mech. Engrg.* 295, 347–361, 2015.

- [6] J. L. Berry, A. Santamarina, J. E. Moore Jr., S. Roychowdhury, W. D. Routh. Experimental and Computational Flow Evaluation of Coronary Stents. *Annal of Biomedical Engineering*, 28, 386–398, 2000.
- [7] N. W. Bressloff, G. Ragkousis, N. Curzen. Design Optimisation of Coronary Artery Stent Systems. *Ann. Biomed. Eng.* 44 (2), 357–367, 2016.
- [8] F. Brezzi, M. Fortin. Mixed and Hybrid Finite Element Methods. Springer, 1991.
- [9] D. Q. Cao, R. W. Tucker. Nonlinear dynamics of elastic rods using the Cosserat theory: Modelling and simulation. *International Journal of Solids and Structures* 45 (2), pp. 460–477, 2007.
- [10] M. A. Costa. Molecular Basis of Restenosis and Drug-Eluting Stents. *Circulation* 111(17), 2257–2273, 2005.
- [11] S. Čanić, M. Galović, M. Ljulj, J. Tambača. A dimension-reduction based coupled model of mesh-reinforced shells. SIAM J Applied Mathematics 77(2), 744–769, 2017.
- [12] S. Čanić, J. Tambača. Cardiovascular Stents as PDE Nets: 1D vs. 3D, IMA Journal of Applied Mathematics 77, 6, 748–779, 2012.
- [13] M. Caputo, C. Chiastra, C. Cianciolo, E. Cutri, G. Dubini, J. Gunn, B. Keller, P. Zunino. Simulation of oxygen transfer in stented arteries and correlation with in-stent restenosis. *International journal for numerical methods in biomedical engineering* 29(12) 1373–87, 2013.
- [14] E. Cutri, P. Zunino, S. Morlacchi, C. Chiastra, F. Migliavacca. Drug delivery patterns for different stenting techniques in coronary bifurcations: a comparative computational study. *Biomech Model Mechanobiol.* 12(4), 657–69, 2013.
- [15] H. Deng, L. Cheng, X. Liang, D. Hayduke, A. C. To. Topology optimization for energy dissipation design of lattice structures through snap-through behavior. *Comput. Methods* Appl. Mech. Engrg. 358, 112641, 28 pp., 2020.
- [16] H. Deng, S. Hinnenbush, A. C. To. Topology optimization of stretchable metamaterials with Bezier skeleton explicit density (BSED) representation algorithm. *Comput. Methods Appl. Mech. Engrg.* 366, 113093, 28 pp., 2020.
- [17] C. Dumoulin, B. Cochelin. Mechanical behaviour modelling of balloon-expandable stents. Journal of Biomechanics 33 (11), 1461–1470, 2000.
- [18] A. O. Frank, P. W. Walsh and J. E. Moore Jr.. Computational Fluid Dynamics and Stent Design. *Artificial Organs* 26 (7), 614–621, 2002.
- [19] J. Frischkorn, S. Reese. Solid-beam finite element analysis of Nitinol stents. *Comput. Methods Appl. Mech. Engrg.* 291, 42–63, 2015.
- [20] G. Griso, Asymptotic behavior of structures made of curved rods. *Anal. Appl. (Singap.)* 6 (2008), 11–22.
- [21] L. Grubišić, J. Iveković, J. Tambača, B. Žugec, Mixed formulation of the one-dimensional equilibrium model for elastic stents. *Rad HAZU* 21 (2017), 219–240.
- [22] L. Grubišić, J. Tambača, Direct solution method for the equilibrium problem for elastic stents. *Numerical Linear Algebra with Applications* 26, 3, e2231, 2019.

- [23] J. Iqbal, J. Gunn, P. W. Serruys. Coronary stents: historical development, current status and future directions. *British Medical Bulletin* 106(1), 193–211, 2013.
- [24] K. A. James, H. Waisman. Layout design of a bi-stable cardiovascular stent using topology optimization. Comput. Methods Appl. Mech. Engrg. 305, 869–890, 2016.
- [25] M. Jurak, J. Tambača. Derivation and justification of a curved rod model. *Mathematical Models and Methods in Applied Sciences* 9, 991–1014, 1999.
- [26] M. Jurak, J. Tambača. Linear curved rod model. General curve. Mathematical Models and Methods in Applied Sciences 11, 1237–1252, 2001.
- [27] G. S. Karanasiou, M. I. Papafaklis, C. Conway, L. K. Michalis, R. Tzafriri, E. R. Edelman, D. I. Fotiadis. Stents: Biomechanics, Biomaterials, and Insights from Computational Modeling. Ann. Biomed. Eng. 45(4), 853–872, 2017.
- [28] A. Kastrati, J. Dirschinger, P. Boekstegers, S. Elezi, H. Schühlen, J. Pache, G. Steinbeck, C. Schmitt, K. Ulm, F. J. Neumann, A. Schömig. Influence of Stent Design on 1-Year Outcome after Coronary Stent Placement: A Randomized Comparison of Five Stent Types in 1,147 Unselected Patients. Catheter. Cardiovasc. Interv. 50(3), 290–297, 2000.
- [29] H. Kawamoto, V. F. Panoulas, K. Sato, T. Miyazaki, T. Naganuma, A. Sticchi, F. Figini, A. Latib, A. Chieffo, M. Carlino, M. Montorfano, A. Colombo. Impact of Strut Width in Periprocedural Myocardial Infarction. *JACC: Cardiovascular Interventions* 8 (7), 900–909, 2015.
- [30] K. W. Lau, A. Johan, U. Sigwart and J. S. Hung. A stent is not just a stent: stent construction and design do matter in its clinical performance. Singapore Medical Journal 45 (7), 305–312, 2004.
- [31] F. Migliavacca, L. Petrini, M. Colombo, F. Auricchio and R. Pietrabissa. Mechanical behavior of coronary stents investigated through the finite element method. *Journal of Biomechanics* 35 (6), 803–811, 2002.
- [32] S. Morlacchi, E. Chiastra, E. Cutri, P. Zunino, F. Burzotta, L. Formaggia, G. Dubini, F. Migliavacca. Stent deformation, physical stress, and drug elution obtained with provisional stenting, conventional culotte and Tryton-based culotte to treat bifurcations: a virtual simulation study. *Eurointervention* 9(12) 1441–53, 2014.
- [33] A. C. Morton, D. Crossman and J. Gunn. The influence of physical stent parameters upon restenosis. *Pathologie Biologie*, 52 (4), 196–205, 2004.
- [34] J. Pache, A. Kastrati, J. Mehilli, H. Schühlen, F. Dotzer, J. Hausleiter, M. Fleckenstein, F. J. Neumann, U. Sattelberger, C. Schmitt, M. Müller, J. Dirschinger, A. Schömig. Intracoronary Stenting and Angiographic Results: Strut Thickness Effect on Restenosis Outcome (ISAR-STEREO) Trial. Circulation 103(23), 2816–2821, 2001.
- [35] J. B. Russ, R. L. Li, A. R. Herschman, H. Waisman, V. Vedula, J. W. Kysar, D. Kalfa. Design optimization of a cardiovascular stent with application to a balloon expandable prosthetic heart valve. *Materials and Design* 209:109997, pp. 20, 2021.
- [36] L. Scardia. The nonlinear bending-torsion theory for curved rods as Γ-limit of three-dimensional elasticity. Asymptotic Analisys 47 (3-4), 317–343, 2006.
- [37] T. Schmidt, J. D. Abbott, Coronary Stents: History, Design, and Construction (Review Article) *Journal of Clinical Medicine* 7(6):126, 2018.

- [38] M. Simoes, E. Martinez-Paneda. Phase field modelling of fracture and fatigue in Shape Memory Alloys. Comput. Methods Appl. Mech. Engrg. 373, 113504, 2020.
- [39] J. Tambača, M. Kosor, S. Čanić, D. Paniagua. Mathematical Modeling of Endovascular Stents. SIAM J Appl Math. Volume 70, Issue 6, pp. 1922–1952, 2010.
- [40] J. Tambača, I. Velčić, Derivation of the nonlinear bending-torsion model for a junction of elastic rods, *Proceedings of the Royal Society of Edinburgh, Section: A Mathematics* 142, 633–664, 2012.
- [41] Y. Wang, S. Čanić, M. Bukač, J. Tambača. Fluid-structure interaction between pulsatile blood ow and a curved stented coronary artery on a beating heart: a four stent computational study. *Computer Methods in Applied Mechanics and Engineering* 35(15), 679–700, 2019.
- [42] F. G. P. Welt. Inflammation and Restenosis in the Stent Era. Arterioscler., Thromb., Vasc. Biol. 22(11), 1769–1776, 2002.
- [43] P. Zunino, J. Tambača, E. Cutri, S. Čanić, L. Formaggia, F. Migliavacca. Integrated stent models based on dimension reduction. Review and future perspectives, *Annals of Biomedical Engineering* 44(2), 604–617, 2016.
- [44] P. Zunino, C. D'angelo, L. Petrini, C. Vergara, C. Capelli, F. Migliavacca. Numerical simulation of drug eluting coronary stents: mechanics, fluid dynamics and drug release. *Computer Methods in Applied Mechanics and Engineering* 198 (45-46), 3633–3644, 2009.
- [45] US Food and Drug Administration: Summary of Safety and Effectiveness of Cypher(TM) stent. April 23, 2004.